



# Object-based ensemble estimation of snow depth and snow water equivalent over multiple months in Sodankylä, Finland

David Brodylo<sup>1</sup>, Lauren V. Bosche<sup>1</sup>, Ryan R. Busby<sup>2</sup>, Elias J. Deeb<sup>3</sup>, Thomas A. Douglas<sup>1</sup>, Juha Lemmetyinen<sup>4</sup>

<sup>1</sup>U.S. Army Cold Regions Research and Engineering Laboratory, Fort Wainwright, AK 99709, USA

<sup>2</sup>U.S. Army Construction Engineering Research Laboratory, Champaign, IL 61826, USA

<sup>3</sup>U.S. Army Cold Regions Research and Engineering Laboratory, Hanover, NH 03755, USA

<sup>4</sup>Finnish Meteorological Institute, 00101 Helsinki, Finland

*Correspondence to:* David Brodylo (david.brodylo@usace.army.mil)

**Abstract.** Snowpack characteristics such as snow depth and snow water equivalent (SWE) are widely studied in regions prone to heavy snowfall and long winters. These features are measured in the field via manual or automated observations and over larger spatial scales with stand-alone remote sensing methods. However, individually these methods may struggle with accurately assessing snow depth and SWE in local spatial scales of several square kilometers. One method for leveraging the benefits of each individual dataset is to link field-based observations with high-resolution remote sensing imagery and then employ machine learning techniques to estimate snow depth and SWE across a broader geographic region. Here, we combined field-based repeat snow depth and SWE measurements over six instances from December 2022 to April 2023 in Sodankylä, Finland with Light Detection and Ranging (LiDAR) and WorldView-2 (WV-2) data to estimate snow depth, SWE, and snow density over a 10 km<sup>2</sup> local scale study area. This was achieved with an object-based machine learning ensemble approach by first upscaling more numerous snow depth field data and then utilizing the estimated local scale snow depth to aid in estimating SWE over the study area. Snow density was then calculated from snow depth and SWE estimates. Snow depth peaked in March, SWE shortly after in early April, and snow density at the end of April. The ensemble-based approach had encouraging success with upscaling snow depth and SWE. Associations were also identified with carbon- and mineral-based forest surface soils, alongside dry and wet peatbogs.

## 1 Introduction

Seasonal snow is found in regions of the globe that experience freezing temperatures and is widely studied to monitor changes in climate and hydrology. Snow is a component of the cryosphere that is heterogeneous over space and time. Snowmelt provides drinking and irrigation water to approximately one sixth of the world's population (Barnett et al., 2005). The initial layering of the snowpack is impacted by the deposition of falling snow, windblown snow redistribution, or a combination of the two (Nienow and Campbell, 2011). Further densification can occur due to compaction and metamorphic mechanisms, alongside meltwater, percolation, and refreeze events (Prowse and Owens, 1984; Tuttle and Jacobs, 2019; El Oufir et al., 2021;



31 Colliander et al., 2023). Given these factors, key elements of snow density are the age of the snowpack, snow depth, and water  
32 content. Fresh snow can have a snow density of  $0.05 - 0.07 \text{ g/cm}^3$  while fresh damp snow can range from  $0.10 - 0.20 \text{ g/cm}^3$   
33 (Muskett, 2012). In contrast, the snow density of older dry snow is roughly  $0.35 - 0.40 \text{ g/cm}^3$  and for older wet snow is up to  
34  $0.50 \text{ g/cm}^3$  (Seibert et al., 2015). Very wet snow and firn, which is snow that failed to melt in the previous summer and did not  
35 turn into ice, can contain a snow density ranging from  $0.40 - 0.80 \text{ g/cm}^3$  (Muskett, 2012; Arenson et al., 2021). Within the  
36 northern hemisphere, there is an immense variation in average snow density which ranges from  $0.05 - 0.59 \text{ g/cm}^3$  with an  
37 overall long-term average snow density of  $0.25 \pm 0.07 \text{ g/cm}^3$  (Zhao et al., 2023).

38 Despite the attainability of snow density classification, there are significant complexities with generating the  
39 estimated snow density alongside the related snow depth and snow water equivalent (SWE) over large areas and in challenging  
40 environments such as thick forests and mountainous terrain. Snow depth is simply the total depth of snow on the ground while  
41 SWE can be defined as the resulting depth of water produced from the complete melt of a mass of snow (Henkel et al., 2018).  
42 The quantity of SWE is determined by the amount of snow accumulation alongside the amount of snow melt and sublimation  
43 (Xu et al., 2019). Field-based SWE datasets are both spatially and temporally scarce and can be expensive and labor intensive  
44 to acquire (Henkel et al., 2018; Fontrodona-Bach et al., 2023). In contrast, field-acquired snow depth measurements are more  
45 common, and are both easier and faster to obtain, though their spatial extent is also limited and can be challenging to obtain in  
46 difficult or remote areas (Collados-Lara et al., 2020; Tanniru and Ramsankaran, 2023). Automated stations can be utilized to  
47 collect snow measurements, which are rapidly becoming more commonplace, such as accounting for over 80% of the snow  
48 depth observing network north of  $55^\circ \text{ N}$  in Canada (Brown et al., 2021). However, such stations may sometimes be primarily  
49 intended for non-climatic purposes such as for avalanche warnings and thus not be verified nor corrected for climatic trends  
50 (Salzmann et al., 2014).

51 Alternatives to field-based methods of snow observations are the use of airborne and spaceborne sensors to estimate  
52 snow properties which have achieved great success in recent decades (Nagler and Rott, 2000; Kelly et al., 2003; Marti et al.,  
53 2016; Cimoli et al., 2017; Tsai et al., 2019). Such sensors achieve large spatial coverage and the ability to clearly differentiate  
54 between snow and non-snow features (Nolin, 2010; Raghubanshi et al., 2023). However, many commonly used spaceborne  
55 sensors such as with the Landsat series, the Moderate Resolution Imaging Spectroradiometer (MODIS), the Advanced Very  
56 High Resolution Radiometer (AVHRR), and the Advanced Microwave Scanning Radiometer (AMSR-E/AMSR2) have  
57 limitations. These are either not capable of directly estimating snow depth or SWE, or, if able, have limited penetration or  
58 contain very coarse resolutions that make local scale estimation unattainable, in addition to potential cloud cover contamination  
59 (Rodell and Houser, 2004; Green et al., 2012; Lu et al., 2022; Stillinger et al., 2023). Repeat images captured via airborne  
60 Light Detection and Ranging (LiDAR) can serve to successfully estimate changes in snow depth (Deems et al., 2013; King et  
61 al., 2023); however the flights needed for these are costly, weather dependent, and require trained pilots and LiDAR specialists  
62 (Jacobs et al., 2021; Yu et al., 2022). While issues are present in relying solely on remote sensing for snow depth and SWE  
63 estimation, a blending of remote sensing imagery and field-based snow data can serve to significantly improve snow depth  
64 and SWE estimations (Kongoli et al., 2019; Pulliainen et al., 2020; Cammalleri et al., 2022; Venäläinen et al., 2023).



65 In addition to this, the inclusion of machine learning can expand the potential to estimate snow depth and SWE over  
66 spatial and temporal scales. Machine learning techniques have been successfully applied to predict such features across Earth,  
67 including high altitude and high latitude environments (Jonas et al., 2009; Zhang et al., 2021; Hu et al., 2023). Commonly  
68 employed algorithms including Artificial Neural Network (ANN), K-Nearest Neighbor (KNN), Multiple Linear Regression  
69 (MLR), Random Forest (RF), and Support Vector Machine (SVM) have achieved success in snow depth, SWE, and snow-  
70 liquid ratio estimations (Broxton et al., 2019; Douglas and Zhang, 2021; Ntokas et al., 2021; Hoopes et al., 2023). Individually  
71 many of these algorithms can produce positive results, though there may be a tendency for disagreement in model accuracy  
72 and outcomes (Li et al., 2023). As an alternative, a weighted ensemble-based empirical model can be utilized to potentially  
73 increase model accuracy, while also reducing estimation error (Douglas and Zhang, 2021; Brodylo et al., 2024). As each  
74 algorithm is optimized differently to generate outputs, each containing their pros and cons, an ensemble approach can improve  
75 feature estimation to ensure optimal results (Pes, 2020). A combination of such machine learning models, remote sensing  
76 imagery, and field-based snow data can thus provide the necessary foundations to map snow features across the cryosphere,  
77 which has been experiencing rising temperatures and increasing climatic uncertainty (Pan et al., 2017; Yang et al., 2020; Santi  
78 et al., 2022).

79 One region where application of such a technique is worthwhile is in northern Europe, particularly in the Lapland  
80 region located largely within the Arctic Circle. The area around Sodankylä, Finland is prone to long, cold winters with abundant  
81 snowfall and both on-the-ground snow depth and SWE measurements are available for multiple months or more. Here, we  
82 sought to utilize an object-based machine learning ensemble approach with a combination of time-series field and automated  
83 snow data, alongside WorldView-2 (WV-2) imagery and LiDAR data to upscale snow depth, SWE, and snow density to a 10  
84 km<sup>2</sup> local scale. This was implemented over six instances from December 2022 to April 2023, with snow estimates matched  
85 to dominant vegetative communities. Field-based snow depth observations were upscaled first, before utilizing the estimated  
86 snow depth to aid in upscaling more limited SWE field data to the local scale, with snow density then being mapped. Distinctive  
87 machine learning algorithms were employed and compared to an ensemble-based technique for both snow depth and SWE  
88 estimation.

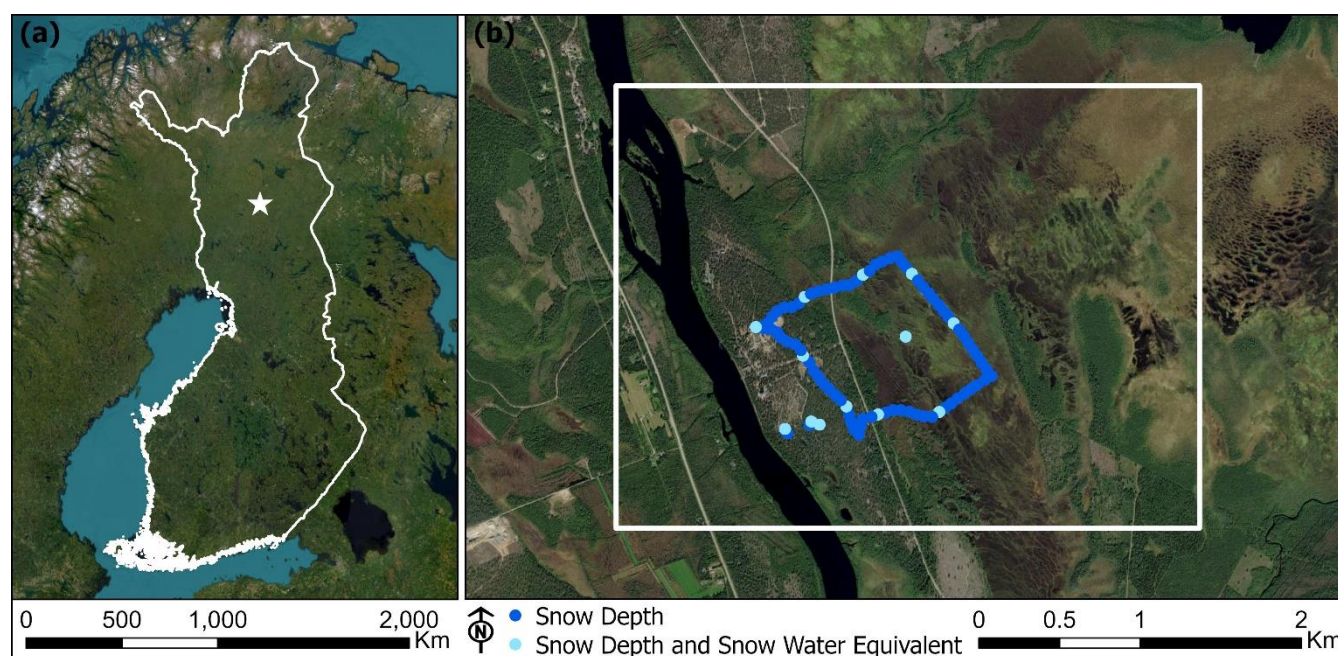
## 89 **2 Study area and data**

### 90 **2.1 Study area**

91 The study area is found near the town of Sodankylä in the Sodankylä municipality of northern Finland, which is  
92 roughly 125 km north of the Arctic Circle. The 10 km<sup>2</sup> site is located along the Kitinen River and hosts the Finnish  
93 Meteorological Institute Arctic Space Centre (FMI-ARC) and the Sodankylä Geophysical Observatory (Bösinger, 2021)  
94 between 67.356° N, 26.609° E, and 67.381° N, 26.693° E (Fig 1). It is largely flat, with elevations ranging between 170 and  
95 190 m above sea level. Landcover consists primarily of coniferous and deciduous dominated forests and peat bogs, contains  
96 organic and mineral soils, and portrays a standard flat northern boreal forest/taiga setting (Rautiainen et al., 2014). Field



97 analysis revealed a multitude of vegetative species at the study site. Dominant tree species are *Betula pubescens* (downy birch)  
 98 and *Pinus sylvestris* (Scots pine). Common shrub species include *Andromeda polifolia* (bog rosemary), *Empetrum nigrum*  
 99 (crowberry), *Rhododendron tomentosum* (Labrador tea), *Vaccinium cespitosum* (dwarf bilberry), *Vaccinium myrtillus*  
 100 (bilberry), *Vaccinium oxycoccus* (cranberry), and *Vaccinium vitis-idaea* (lingonberry). Graminoid species were comprised of  
 101 *Carex lasiocarpa* (woollyfruit sedge), *Danthonia decumbens* (heath grass), *Eriophorum vaginatum* (tussock cottongrass),  
 102 *Scheuchzeria palustris* (pod grass), and *Trichophorum cespitosum* (tufted bulrush). Forb species include *Comarum palustre*  
 103 (purple marshlock) and *Menyanthes trifoliata* (bog bean). Lichen and moss are also common.  
 104

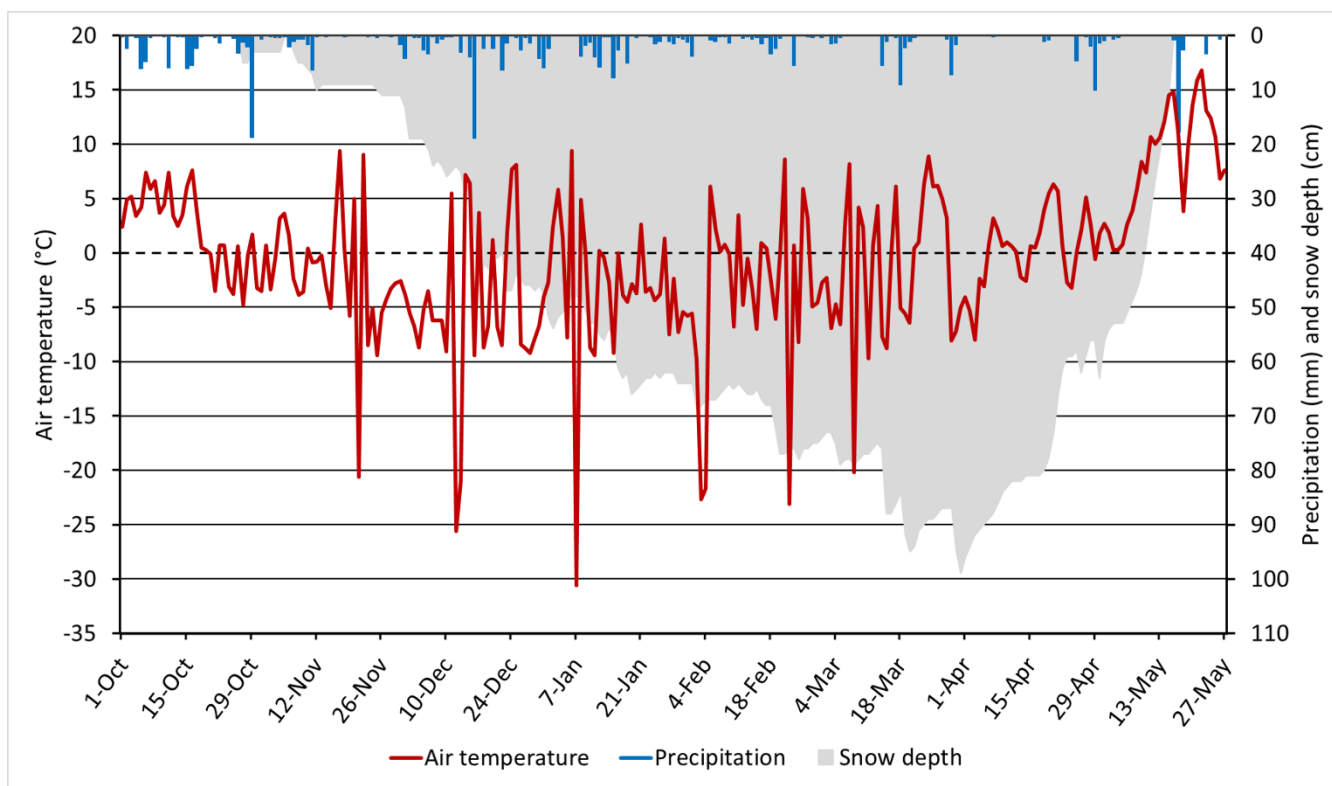


105  
 106 **Figure 1: Study area (a) in Sodankylä, Finland and (b) automated and manual snow depth and snow water equivalent measurements**  
 107 **within the 10 km<sup>2</sup> local scale study site. Image credits: © Esri, Earthstar Geographics, and Maxar.**

108  
 109 The climate in Sodankylä is defined by short but relatively warm summer season and a long and cold winter, with  
 110 snow present from October to May. Taiga snow is dominant, with thick layering of depth hoar at the base of the snowpack  
 111 (Anttila et al., 2014). Meaningful rain-on-snow events occur in November and early December (Bartsch et al., 2023). Between  
 112 1991 and 2020 at the FMI Sodankylä Tähtelä weather station, the average yearly precipitation was 543 mm with an average  
 113 yearly maximum snow depth of 91 cm that ranged from 65 – 127 cm. The average air temperature was 0.4 °C, the average  
 114 minimum was -4.2 °C, and the average maximum was 4.8 °C. The absolute minimum temperature was -49.5 °C while the  
 115 absolute maximum was 32.1 °C. The mean annual air temperature has increased by 0.07 °C from 2000 – 2018 (Bai et al.,  
 116 2021) and is expected to continue. Between the winters of 2007/08 to 2013/14 around FMI-ARC and the Sodankylä  
 117 Geophysical Observatory, the maximum SWE ranged approximately from 150 – 250 mm (Essery et al., 2016). For the winter



118 of 2022/23, a maximum snow depth of 99 cm was recorded at the Sodankylä Tähtelä weather station on 31 March 2023, with  
 119 rapid snow melt in April and early May (Fig 2). The average air temperature was generally near or below freezing in winter  
 120 and contained relatively low precipitation. The site generally contains low wind speeds that limit windblown snow  
 121 redistribution, with a monthly average of 2.5 – 2.9 m s<sup>-1</sup> above the forest canopy (Meinander et al., 2020).  
 122



123  
 124 **Figure 2: Daily average air temperature (°C), precipitation (mm), and snow depth (cm) from the FMI Sodankylä Tähtelä weather**  
 125 **station from 01 October 2022 – 27 May 2023.**

126 **2.2 Ground-based and remotely sensed measurements**

127 Field-based snow data were acquired over distinct vegetative communities on 14 December 2022, 17 January 2023,  
 128 15 February 2023, 17 March 2023, 17 April 2023, and 28 April 2023. Manually obtained snow depth was measured with a  
 129 fixed stake or manual probe, while SWE was calculated with a scale that is paired to a snow tube that is 70 cm high and 10 cm  
 130 in diameter that includes a scale on the outside to measure snow depth (Leppänen et al., 2016). Automated observations were  
 131 performed for snow depth with the Campbell Scientific SR50 sonic distance instrument and for SWE with the Sommer  
 132 Messtechnik SSG 1000 snow scale instrument. A total of 88 repeat snowpack depth (cm) measurements were taken at the  
 133 same locations with 80 being manually recorded and 8 being acquired from automated stations (Fig 1(b)). Of these same 88  
 134 locations, a total of 13 repeat SWE (mm) measurements were recorded: 11 manually and 2 from automated stations. SWE



135 values were based on the total snowpack depth. An average daily value was recorded from the automated stations to match  
136 with the field-based observations, with previously strong correlations found between the automated and manual measurements  
137 for both snow depth and SWE with average correlation coefficients of 0.98 and 0.99, respectively (Leppänen et al., 2018).  
138 Snow density ( $\text{g}/\text{cm}^3$ ) was calculated from dividing SWE by snow depth at the same location.

139 On-the-ground vegetation data were acquired between 31 July and 4 August 2023. Plots were established randomly  
140 along the snow depth measurement route to encompass major plant community types, primarily coniferous and hardwood  
141 forests, and forested and herbaceous bogs. At each plot, a center point was established, flags were placed in each cardinal  
142 direction to create a circular plot with a 7.3 m radius, and GPS coordinates of the center point and flags were recorded. In each  
143 plot, all trees with diameter at breast height (DBH) greater than 10 cm were recorded by species and DBH. Five  $0.5 \text{ m}^2$  quadrats  
144 were randomly placed in each plot quadrant and aerial cover of the understory vegetation was estimated in 5% increments for  
145 the following functional groups: moss, lichen, shrub, forb, and graminoid.

146 Cloud free and high spatial resolution (2 m) spaceborne WV-2 images were acquired on 02 August 2021 and 27 April  
147 2023. The summer imagery contained spectral readings that matched with distinct vegetative communities, while the winter  
148 imagery served to identify snow and non-snow features. Snow-free LiDAR data from 2020 was gathered from the National  
149 Land Survey of Finland at a density of 5 pulses/ $\text{m}^2$ . Airborne LiDAR data were obtained on 27 April and 11 May 2023 by  
150 NV5 Geospatial and contained full to partial snow cover. This was captured with a Leica City Mapper-2/Hypersion 2+ system  
151 containing an average pulse density of  $\geq 25$  pulses/ $\text{m}^2$ , absolute vertical accuracy of  $\leq 6$  cm, relative vertical accuracy of  $\leq 15$   
152 cm, and horizontal accuracy of  $\leq 14$  cm. The LiDAR data were further separated into a Digital Terrain Model (DTM), Digital  
153 Surface Model (DSM), and Canopy Height Model (CHM). No major landcover changes impacted the study site during these  
154 time periods that would have necessitated the need for repeat sets of imagery.

155 Land Use Land Cover (LULC) data were acquired from CORINE (Coordination of Information on the Environment)  
156 Land Cover (CLC) at 20 m resolution from 2018. CLC is a LULC monitoring program that is coordinated by the European  
157 Environment Agency (EEA) and is a current product of the Copernicus Land Monitoring Service (Aune-Lundberg and Strand,  
158 2021). The LULC data was utilized to link vegetative communities to snow depth and SWE in the study area, while excluding  
159 artificial features and water bodies. We downscaled the dataset to match the 2 m resolution WV-2 imagery and then updated  
160 land cover boundaries where there were evident differences with the obtained summer imagery, thereby providing an updated,  
161 higher-resolution LULC. In addition, a modified classification scheme was employed that sought to separate forest  
162 communities by soil type and wetlands by moisture content. A RF-based classification scheme was employed that achieved  
163 an Overall Accuracy (OA) of 91.7% and a Kappa value of 0.91, which indicated high LULC classification accuracy.



## 164 **3 Methodology**

### 165 **3.1 Image segmentation**

166 An Object-Based Image Analysis (OBIA) technique was utilized to make estimations of snow depth and SWE at the  
167 10 km<sup>2</sup> local site scale. In OBIA an image is separated into homogeneous groups of pixels known as image objects or segments,  
168 which are then utilized as the spatial unit for image assessment (Ye et al., 2018). This contrasts with more traditional pixel-  
169 based classification methods, in which image assessment is performed on a pixel-by-pixel basis. The OBIA approach was  
170 selected as it has been found to deliver enhanced accuracy and results over traditional pixel-based approaches, especially with  
171 high-resolution imagery (Sibaruddin et al., 2018; Shayeganpour et al., 2021; Ez-zahouani et al., 2023). Additionally, outputs  
172 generated from traditional pixel-based approaches can be susceptible to high local spatial heterogeneity between adjacent  
173 pixels, commonly known as the “salt-and-pepper” effect, which is not evident with OBIA (Wang et al., 2020).

174 Image segmentation was accomplished with the Segment Mean Shift tool in ArcGIS Pro software, a desktop GIS  
175 application. It contains a nonparametric iterative technique that utilizes kernel density estimation to generate image objects  
176 from a maximum of three image bands by grouping nearby pixels that contain similar spectral characteristics (Goldberg et al.,  
177 2021). The red, green, and near-infrared bands were utilized from the summer WV-2 imagery to carry out image segmentation.  
178 For parameters, the spectral detail was set to 19 (near maximum) while spatial detail was set to 1 (minimum) to improve  
179 segmentation as both heterogeneous and homogenous areas were present. A total of 37,917 unique image objects were created.  
180 Mean and standard deviation were calculated for each image object from the LiDAR and WV-2 datasets. Additional indices  
181 utilized included the Green Chlorophyll Index (GCI), Red-Edge Chlorophyll Index (RECI), Normalized Difference Vegetation  
182 Index (NDVI), Normalized Difference Water Index (NDWI), and Soil-Adjusted Vegetation Index (SAVI). Descriptions of  
183 these widely utilized indices, beyond the scope of this work, are available in Gaitán et al. (2013), Xue and Su. (2017), and  
184 Nadjla et al. (2022). The automated and field-based snow depth and SWE measurements were spatially joined to the generated  
185 image objects. In segments that contained two or more measurements, an average value was recorded.

### 186 **3.2 Machine learning models**

187 Commonly utilized and unique supervised regression-based machine learning models entailing of Random Forest  
188 (RF), Support Vector Machine (SVM), Artificial Neural Network (ANN), and Multiple Linear Regression (MLR) were chosen  
189 to estimate snow depth and SWE for the image objects. RF works by training a large collection of decision trees to generate  
190 an optimal output (Hwang et al., 2023). In contrast, SVM relies on an optimal hyperplane that minimizes error bounds  
191 (Pimentel et al., 2021). ANN is based upon the association of connected neurons like that of the human nervous system (Goel  
192 et al., 2023). MLR models the linear relationship between independent variables to a dependent variable (Kim et al., 2020).  
193 To aid in reducing potential modeling bias and overfitting, a *k*-fold cross-validation technique was employed. With this,  
194 matched data samples are randomly split into *k* number of subsets, with *k*-1 being utilized to train models and the remainder



195 to test models (Abriha et al., 2023). Here, a  $k$ -fold of 10 was utilized whereby in each subset 90% of the data is assigned for  
196 training and 10% is for testing, with output metrics determined from the average of all iterations.

### 197 3.3 Object-based ensemble machine learning

198 An object-based ensemble machine learning approach was applied from a combined weighted output of the RF, SVM,  
199 ANN, and MLR models which is referred to here as Ensemble Analysis (EA). Given that these individual models compute  
200 predictions differently and will have varying accuracies and errors, EA can result in a more robust model that considers more  
201 accurate models while minimizing the influence of less accurate ones. This is relevant for repeat predictions over the same  
202 study site as a model may perform well in one scenario while underperforming in another, such as with estimating snow depth  
203 during a period of low or high snowfall. All four models were included to estimate snow depth, while SVM was dropped for  
204 SWE estimation due to poor modeling results. The model weights for EA were determined by the correlation coefficient ( $r$ ),  
205 in which a model with a larger  $r$  value would be given a higher weight, and the sum of weights equal to 1.0 (Zhang et al.,  
206 2020). Combined model uncertainty for EA predictions was based on the standard deviation of model outputs and is referred  
207 to as the standard deviation to ensemble prediction (STDE). Other statistical metrics included the Mean Absolute Error (MAE),  
208 which is the absolute error between the observed and predicted values, and the Root Mean Square Error (RMSE), which is  
209 more sensitive to outliers and is the square root of the mean squared error between observed and predicted values. Larger  
210 differences between MAE and RMSE would serve to indicate a high variance of the individual errors from the test samples.  
211 The  $r$ , MAE, and RMSE were calculated by:

$$212 \quad r = \frac{\sum_{i=1}^n (p_i - \bar{p}_i)(o_i - \bar{o}_i)}{\sqrt{\sum_{i=1}^n (p_i - \bar{p}_i)^2} \sqrt{\sum_{i=1}^n (o_i - \bar{o}_i)^2}}, \quad (1)$$

$$213 \quad MAE = \frac{\sum_{i=1}^n |p_i - o_i|}{n}, \quad (2)$$

$$214 \quad RMSE = \sqrt{\frac{\sum_{i=1}^n (p_i - o_i)^2}{n}}, \quad (3)$$

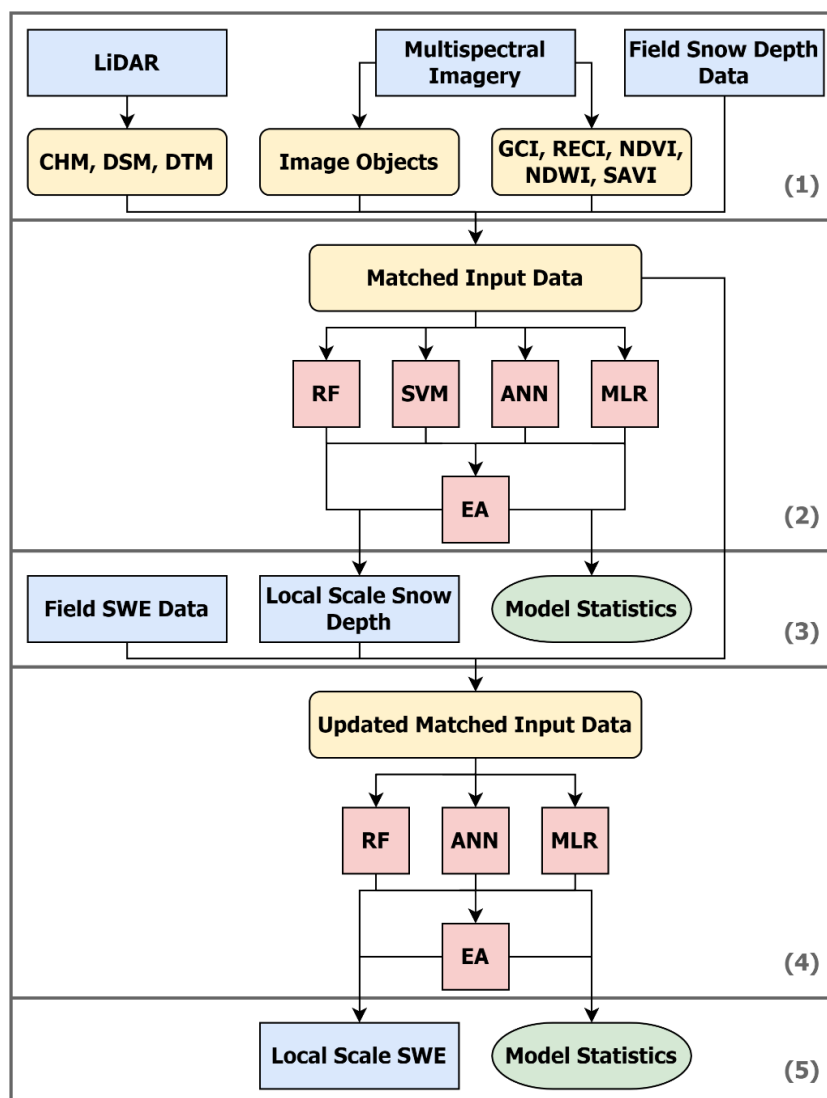
215 where  $n$  is the number of matched samples,  $p_i$  is the model prediction,  $o_i$  is the observed snow depth or SWE,  $\bar{p}_i$  is the average  
216 of the predicted values, and  $\bar{o}_i$  is the average of the observed snow depth or SWE as adapted from Brodylo et al. (2024).

217 Local scale estimations were generated for snow depth via the ensemble-based approach, which were then utilized as  
218 added inputs to aid in upscaling the more limited field acquired SWE data to the same local scale. Snow density was measured  
219 by dividing the estimated SWE by the estimated snow depth in each respective instance. A summary of the methodology  
220 framework can be found in Fig 3. Image objects were generated from multispectral imagery via image segmentation, with  
221 averaged remote sensing and field snow depth values assigned to each unique image object (1). The spatially matched data  
222 was then evaluated through the base machine learning models (RF, SVM, ANN, and MLR) to predict snow depth before being  
223 ascertained with EA by combining model outputs with weighted averaging based on the  $r$  value of each model (2). Model





224 metrics were obtained from each model alongside the mapped estimated local scale snow depth, with the estimated snow depth  
 225 from EA and field SWE values then being spatially joined to the previously matched input data (3). The updated spatially  
 226 matched data was analyzed by the base machine learning models (RF, ANN, and MLR) to predict SWE before being finalized  
 227 with EA (4). Model metrics were generated along with the mapped estimated local scale SWE in each instance (5).  
 228



229  
 230 **Figure 3: Methodology framework to upscale field snow depth data to a local scale by using an object-based ensemble machine**  
 231 **learning approach, and then joining the produced snow depth outputs and matched input data with the field SWE data to generate**  
 232 **local scale SWE outputs. Blue indicates input/output data, yellow indicates processed data, red indicates machine learning, and**  
 233 **green indicates model metrics. RF is Random Forest, SVM is Support Vector Machine, ANN is Artificial Neural Network, MLR is**  
 234 **Multiple Linear Regression, and EA is Ensemble Analysis.**



235 While the methodology is similar to that found in Brodylo et al. (2024), that work was solely intent on upscaling 1  
236 m<sup>2</sup> permafrost active layer thickness (ALT) field data to three 1 km<sup>2</sup> local scale sites in Alaska before then further upscaling  
237 the ALT estimates to a 100 km<sup>2</sup> regional scale over multiple years. Here, we focused on first upscaling repeat field snow depth  
238 measurements to a 10 km<sup>2</sup> local scale in Finland over multiple instances, and then combined the estimated snow depth data to  
239 the original machine learning input data. The addition of snow depth as an input variable enabled a separate, enhanced estimate  
240 of SWE at the same 10 km<sup>2</sup> local scale with more limited repeat field SWE measurements over the same multiple instances in  
241 a single winter period. This then permitted snow density to be calculated at each moment in time from snow depth and SWE  
242 estimations. The approach was applied to a shorter temporal analysis for snow depth, SWE, and snow density. It revealed how  
243 each of these variables were interconnected during the initial, middle, and late winter, how machine learning models performed  
244 over the course of the winter period, and how the studied variables related to landcover types over these different instances. In  
245 addition, machine learning snow depth estimates were directly compared to independent LiDAR-based snow depth estimation.

## 246 4 Results

### 247 4.1 Snow depth

248 All tested models performed relatively well with the snow depth estimations. The best  $r$ , MAE, and RMSE values  
249 were observed with EA in all instances (Table 1). March and April contained the highest  $r$  values which were above or equal  
250 to 0.67, and peaked with EA at 0.80 in March, 0.75 in early April, and 0.79 at the end of April. December, which had the  
251 lowest snow depth, had the worst  $r$  values with a minimum of 0.46 produced with ANN and a maximum of 0.63 produced  
252 with EA. Owing to the lower snow depth, MAE and RMSE were the smallest out of all six instances at 2.8 cm and 3.6 cm for  
253 EA, respectively. MAE and RMSE steadily increased for all models from roughly 2.8 – 3.3 cm and 3.6 – 4.4 cm in December  
254 to 5.9 – 7.1 cm and 7.8 – 8.9 cm at the end of April. This was expected given increased snowfall and snow depth over time,  
255 alongside minor periods of snowmelt throughout and accelerated snowmelt in April that would increase model uncertainty.  
256 The base models of RF, SVM, ANN, and MLR generally contained similar values for each instance, with some variation. RF  
257 and SVM performed well in all instances, though the former produced the worst  $r$  (0.66) in January while the latter produced  
258 consistently above average  $r$ , MAE, and RMSE values in all instances. ANN generated the poorest outcomes for  $r$ , MAE, and  
259 RMSE (0.46, 3.3 cm, and 4.4 cm) in December, however outside of that it produced positive results, such as in January where  
260 it produced the best for all three (0.69, 3.9 cm, and 4.8 cm). MLR performed on par with the other machine learning algorithms,  
261 yet it arguably produced the poorest metrics, as it repeatedly delivered the highest MAE and RMSE in February (4.9 and 5.9  
262 cm), March (4.8 and 6.0 cm), early April (6.4 and 8.4 cm), and the end of April (7.1 and 8.9 cm). More information about  
263 outputs produced with EA for each instance can be seen in Fig 4, with each instance containing a 1:1 line, fitted linear  
264 regression line, and scatterplot with STDE error bars in blue. With minor exceptions, there was largely an overall agreement  
265 between the field and estimated snow depth values, and between the individual model outputs.

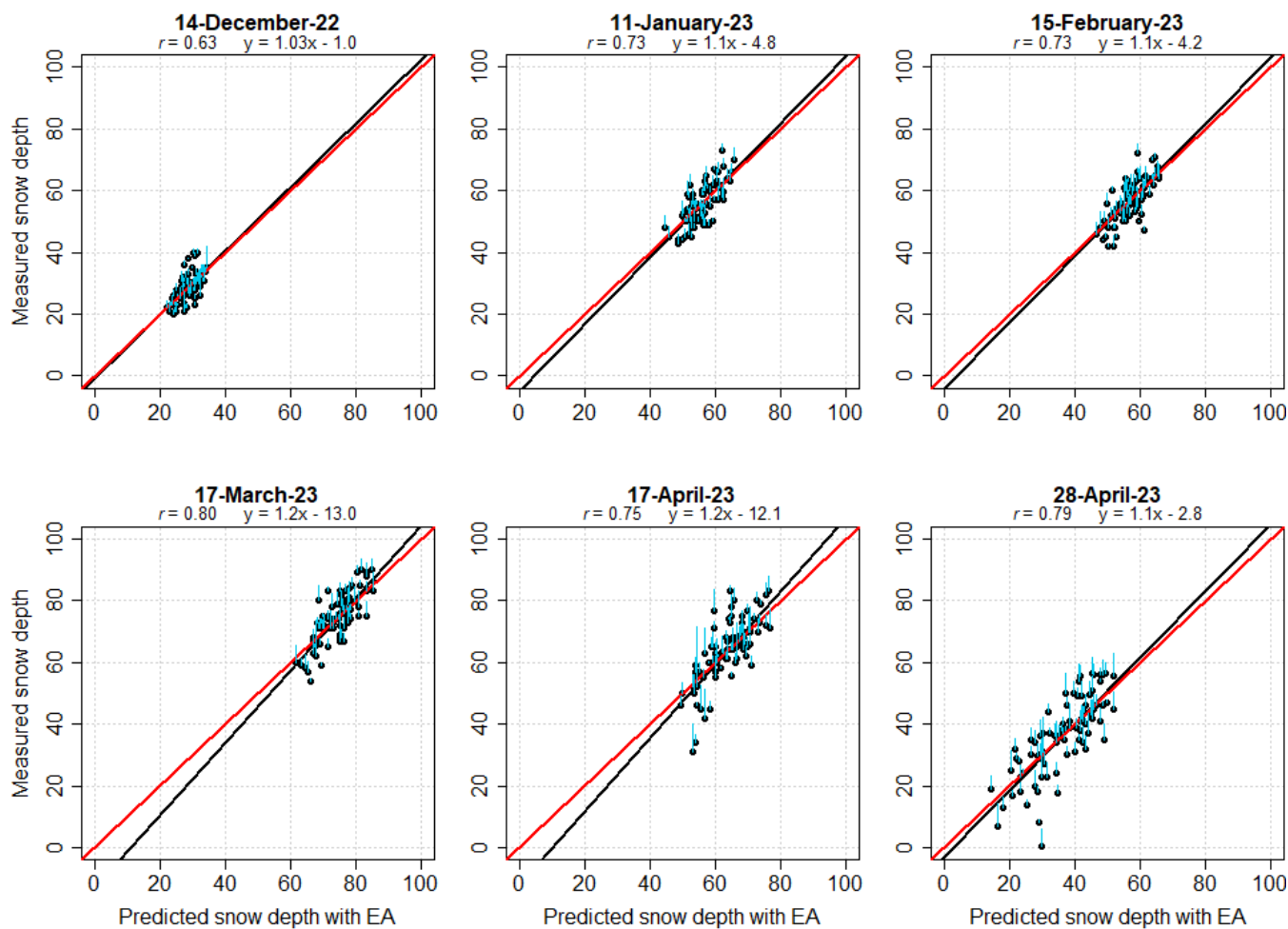


266  
267

**Table 1: Machine learning model metrics for estimated snow depth with RF, SVM, ANN, MLR, and EA. MAE and RMSE are in cm.**

14-December-22						17-January-23					
	RF	SVM	ANN	MLR	EA		RF	SVM	ANN	MLR	EA
<i>r</i>	0.60	0.61	0.46	0.56	0.63	<i>r</i>	0.66	0.69	0.69	0.68	0.73
MAE	2.9	2.8	3.3	3.2	2.8	MAE	4.1	4.0	3.9	4.0	3.7
RMSE	3.7	3.7	4.4	4.2	3.6	RMSE	4.9	4.9	4.8	5.1	4.5
15-February-23						17-March-23					
	RF	SVM	ANN	MLR	EA		RF	SVM	ANN	MLR	EA
<i>r</i>	0.73	0.73	0.67	0.62	0.73	<i>r</i>	0.78	0.78	0.70	0.72	0.80
MAE	3.9	3.7	4.1	4.9	3.6	MAE	4.4	4.0	4.6	4.8	3.9
RMSE	4.8	4.7	5.1	5.9	4.6	RMSE	5.4	5.1	5.7	6.0	4.9
17-April-23						28-April-23					
	RF	SVM	ANN	MLR	EA		RF	SVM	ANN	MLR	EA
<i>r</i>	0.67	0.68	0.68	0.67	0.75	<i>r</i>	0.76	0.74	0.74	0.73	0.79
MAE	5.7	5.7	5.8	6.4	5.1	MAE	6.1	6.4	6.6	7.1	5.9
RMSE	7.9	7.9	7.7	8.4	7.1	RMSE	8.2	8.5	8.5	8.9	7.8

268



269

270

271

272

**Figure 4: Scatterplot, 1:1 line (red line), and fitted regression line (black line) between the predicted snow depth from EA and the measured snow depth on each occasion from 14-December-2022 until 28-April-2023. STDE is in cyan.**

273

274

275

276

277

278

279

280

281

The snow depth average and standard deviation at each of the vegetative land cover types with the field data and local scale EA outputs are in Table 2. Mapped snow depth at the field scale and local scale estimates with EA for each instance from December 2022 – April 2023 can be seen in Fig 5. There was a general agreement and similar snow depth patterns in LULC's that contained both field and local scale data. The average snow depth was lowest for the field and local scale in December at 29 cm for both, while the highest readings were in March at 75 and 76 cm, with a rapid decline at the end of April at 36 and 37 cm. Standard deviation was lowest in December ( $\pm 5$  and  $\pm 3$  cm) while highest at the end of April ( $\pm 13$  and  $\pm 8$  cm) when there was increased snowmelt. At the field scale there was up to a 10 – 11 cm difference between coniferous forest (peat soil) and coniferous forest (mineral soil) from January to early April. The exception is at the end of April during the period of



282 snowmelt when field coniferous forest (mineral soil) contained higher snow depth at 43 cm than coniferous forest (peat soil)  
283 at 40 cm. A similar pattern was evident with the field transitional woodland/shrub (peat soil) repeatedly containing higher  
284 snow depths than transitional woodland/shrub (mineral soil) with a maximum difference of 10 cm in early April. However, at  
285 the end of April both were equal at 36 cm of snow depth. Field-based peatbog (wet) and open area contained the lowest levels  
286 of snow depth in all instances, ranging from 26 – 70 cm and 25 – 70 cm, respectively, with the latter experiencing elevated  
287 standard deviation of  $\pm 20$  and  $\pm 22$  cm in the last two instances.

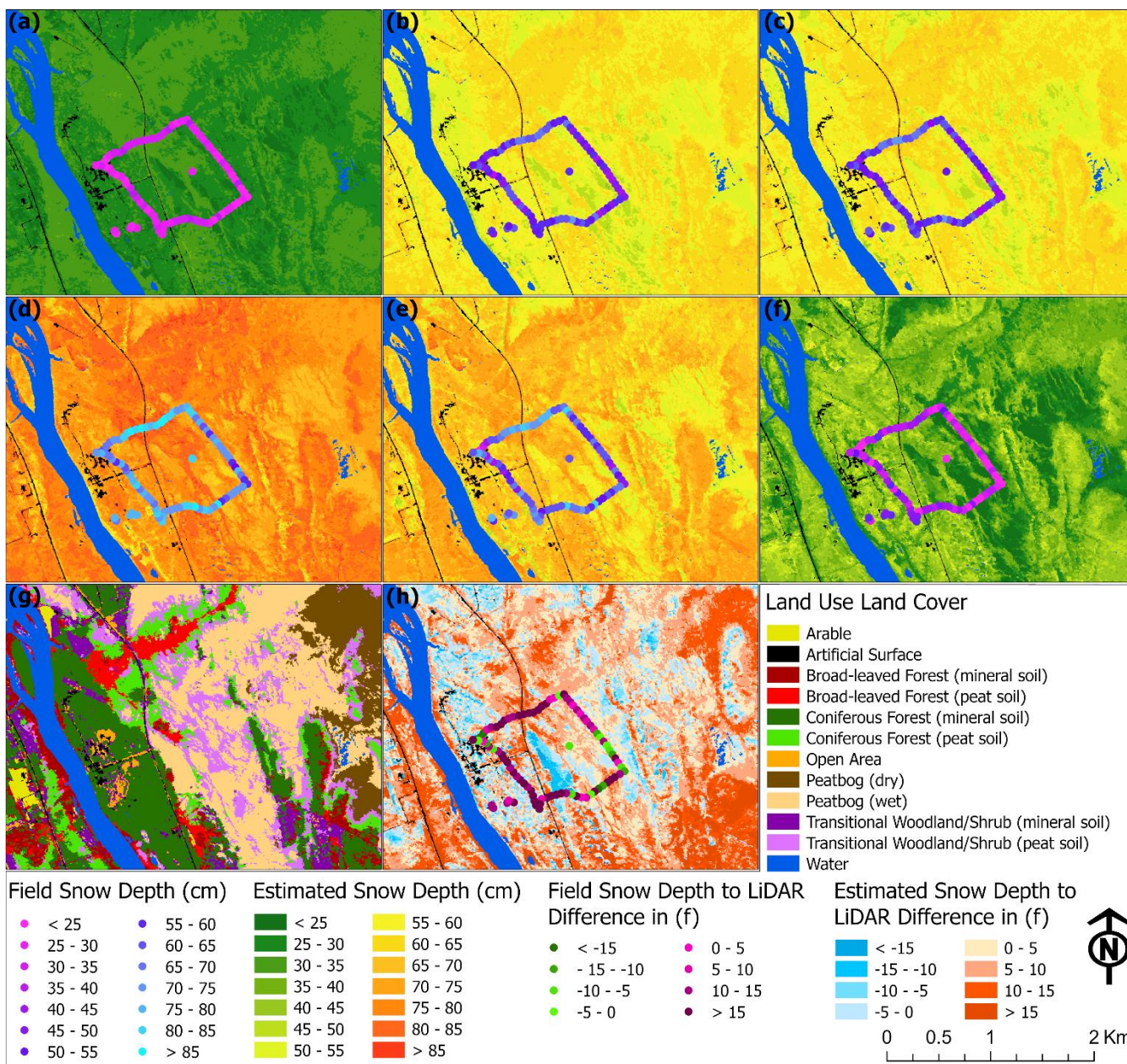


288  
289

**Table 2: Mean and standard deviation (in parentheses) for snow depth (cm) estimates per LULC with field data and at the local scale with EA. Blank values indicate no field data.**

	Snow depth field data						Snow depth estimates with EA					
	14-Dec-22	17-Jan-23	15-Feb-23	17-Mar-23	17-Apr-23	28-Apr-23	14-Dec-22	17-Jan-23	15-Feb-23	17-Mar-23	17-Apr-23	28-Apr-23
Arable							29	60	61	77	69	37
							(3)	(6)	(6)	(6)	(5)	(9)
Broad-leaved forest (mineral soil)							31	60	60	77	71	41
							(2)	(3)	(3)	(4)	(4)	(6)
Broad-leaved forest (peat soil)							32	61	61	79	70	40
							(2)	(3)	(3)	(3)	(4)	(6)
Coniferous forest (mineral soil)	29	55	57	74	64	43	29	57	58	75	66	40
	(5)	(6)	(4)	(6)	(7)	(9)	(2)	(4)	(3)	(5)	(4)	(5)
Coniferous forest (peat soil)	34	66	67	84	74	40	32	63	63	81	72	42
	(2)	(5)	(5)	(6)	(7)	(2)	(1)	(3)	(2)	(3)	(3)	(5)
Open area	25	54	54	70	51	33	28	60	61	77	67	39
	(4)	(7)	(6)	(7)	(20)	(22)	(3)	(5)	(4)	(5)	(6)	(7)
Peatbog (dry)							30	59	59	73	63	36
							(2)	(3)	(3)	(3)	(5)	(5)
Peatbog (wet)	26	52	53	70	61	27	27	56	56	73	61	30
	(4)	(6)	(8)	(9)	(10)	(12)	(2)	(4)	(4)	(5)	(6)	(7)
Transitional woodland /shrub (mineral soil)	29	57	57	74	60	36	30	61	61	79	70	41
	(2)	(6)	(5)	(7)	(14)	(14)	(3)	(4)	(4)	(5)	(6)	(7)
Transitional woodland /shrub (peat soil)	31	59	61	80	70	37	30	61	61	79	69	39
	(5)	(6)	(7)	(6)	(8)	(9)	(2)	(4)	(4)	(5)	(5)	(7)
All LULC	29	56	57	75	64	36	29	58	59	76	66	37
	(5)	(7)	(7)	(8)	(11)	(13)	(3)	(5)	(4)	(5)	(7)	(8)

290



291 **Figure 5: Field and estimated snow depth (cm) in a) 14-December-22, b) 17-January-23, c) 15-February-23, d) 17-March-23, e) 17-**  
 292 **April-23, and f) 28-April-23 alongside g) a LULC map based on data from CLC and h) 28-April-23 snow depth difference from 27-**  
 293 **April-23 collected LiDAR.**  
 294

295  
 296 At peak snow depth at the local scale in March, both dry and wet peatbogs contained the lowest average snow depth  
 297 at 73 cm. Dry, unsaturated peatbog was found to have snow depths equal to or greater than wet, saturated peatbog, with a



298 difference of 3 cm in the first three months, equal in March and early April, and then jumping to 6 cm at the end of April  
299 during more intense snow melt. Arable and open area contained similar estimated snow depth values in all instances and were  
300 higher than dry and wet peatbogs from January to the end of April. Forests and transitional woodlands largely contained the  
301 highest average values in March with broad-leaved forest recording 77 cm (mineral soil) and 79 cm (peat soil), coniferous  
302 forest (peat soil) with 81 cm, and transitional woodland/shrub containing 79 cm in both mineral and peat soil. There was also  
303 a consistent 1-2 cm snow depth difference between the local scale broad-leaved forest peat soils and mineral soils, with the  
304 former having higher snow depth leading up to peak snow depth in March, while the inverse was evident post peak snow  
305 depth. Transitional woodland/shrub mimicked this during post peak snow depth with a 1-2 cm snow depth difference between  
306 mineral and peat soil. Local scale coniferous forest (peat soil) consistently contained snow depth values greater than coniferous  
307 forest (mineral soil), with up to a 5 – 6 cm difference from January to early April. In addition, field and local scale snow depth  
308 estimates from 28 April were compared to the difference between snow covered DTM from the prior day and snow-free DTM  
309 from 2020. Results indicate field snow depth measurements generally exceeded the estimated LiDAR-based snow depth  
310 estimations by an average of 9.6 cm, while for the local scale with EA it was lower at 5.4 cm.

#### 311 **4.2 Snow water equivalent**

312 Machine learning model performance for SWE estimation between RF, ANN, MLR, and EA can be seen in Table 3.  
313 Given more limited field-based SWE measurements with 13 samples, the models encountered more pronounced challenges  
314 matching estimations to real-world data yet were generally able to produce acceptable results. SVM was dropped due to poor  
315 performance in all instances. ANN, MLR, and EA contained relatively stable and positive metrics for  $r$ , MAE, and RMSE in  
316 all instances. EA generally produced the best metrics, although MLR performed best in some instances. Metrics from RF  
317 varied considerably, being on-par with the other models in December, February, and late April while poor in January, March,  
318 and early April. Despite this, RF was included in the weighted ensemble procedure given that in some instances it produced  
319 acceptable outcomes, while in others the low  $r$  value would greatly minimize its weight. A scatterplot, 1:1 line, and fitted linear  
320 regression line for each instance of SWE predictions produced by EA alongside STDE can be seen in Fig 6. December  
321 contained the poorest metrics, with a maximum  $r$  of 0.37 with MLR and EA, which may be connected to the poorer snow  
322 depth metrics in that same month, while March contained the highest  $r$  of 0.87 with MLR and 0.79 with EA. Similarly with  
323 the snow depth metrics over the same period, MAE and RMSE were lowest in December from roughly 5.0 – 6.6 mm and 5.9  
324 – 7.9 mm before rising to become the highest at the end of April at 24.1 – 33.4 mm and 33.4 – 41.5 mm.



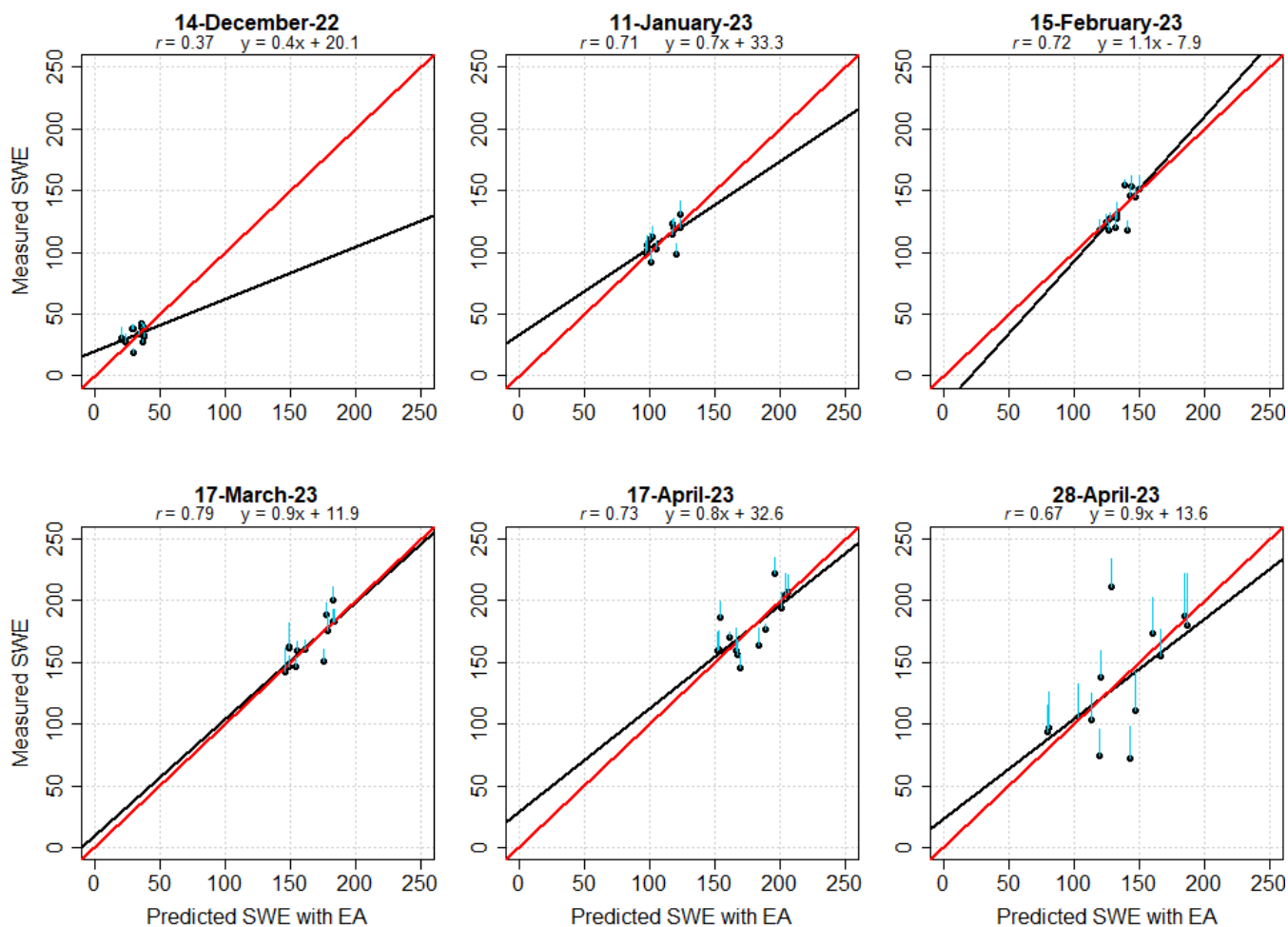


325  
326

**Table 3: Machine learning model metrics for estimated snow water equivalent with RF, ANN, MLR, and EA. MAE and RMSE are in mm.**

14-December-22					17-January-23				
	RF	ANN	MLR	EA		RF	ANN	MLR	EA
<i>r</i>	0.30	0.36	0.37	0.37	<i>r</i>	0.05	0.69	0.63	0.71
MAE	5.0	6.2	6.6	5.8	MAE	9.0	8.4	6.9	6.7
RMSE	5.9	7.5	7.9	6.6	RMSE	11.0	10.5	9.6	8.4
15-February-23					17-March-23				
	RF	ANN	MLR	EA		RF	ANN	MLR	EA
<i>r</i>	0.71	0.67	0.70	0.72	<i>r</i>	0.16	0.64	0.87	0.79
MAE	11.0	8.9	8.3	6.7	MAE	15.2	12.0	6.3	8.2
RMSE	12.3	11.6	10.9	9.8	RMSE	17.4	16.0	8.7	10.9
17-April-23					28-April-23				
	RF	ANN	MLR	EA		RF	ANN	MLR	EA
<i>r</i>	0.09	0.70	0.72	0.73	<i>r</i>	0.55	0.56	0.71	0.67
MAE	19.4	14.9	12.9	13.5	MAE	33.4	30.5	31.2	24.1
RMSE	22.5	18.0	16.0	15.8	RMSE	39.2	41.5	36.9	33.4

327



328

329 **Figure 6: Scatterplot, 1:1 line (red line), and fitted regression line (black line) between the predicted SWE from EA and the measured**  
330 **SWE on each occasion from 14-December-2022 until 28-April-2023. STDE is in cyan.**

331

332 The  $r$  values produced by RF ranged from a very poor correlation of 0.05 in January to a high correlation of 0.71 in  
333 February. Despite this, RF easily contained the best MAE and RMSE from all models in December (5.0 and 5.9 mm) alongside  
334 the best  $r$  in February from all base models at 0.71, with EA at 0.72. ANN primarily contained metrics that were intermediate,  
335 yet from the base models it was able to produce in January the best  $r$  at 0.69 and in late April the best MAE at 30.5. Out of the  
336 base models, MLR generally achieved the best  $r$ , MAE, and RMSE in most instances, with it being especially dominant in  
337 March (0.87, 6.3 mm, and 8.7 mm) and early April (0.72, 12.9 mm, and 16.0 mm). However, it also produced the worst MAE  
338 and RMSE in December (6.2 and 7.9 mm). In contrast, EA continually generated the best or second-best metrics in all instances  
339 for  $r$ , MAE, and RMSE. EA was particularly dominant with the best  $r$ , MAE, and RMSE in January (0.71, 6.7 mm, 8.4 mm)  
340 and February (0.72, 6.7 mm, 9.8 mm). This was despite the large variation in  $r$  for RF in both months (0.05 and 0.71). In



341 December it matched MLR for the highest  $r$  (0.37), while in early April it contained slightly better  $r$  (0.73) and RMSE (15.8).  
342 At the end of April, EA generated the lowest MAE (24.1 mm) and RMSE (33.4 mm), which were notably better than the best  
343 base model MAE from ANN (30.5 mm) and RMSE from MLR (36.9 mm).

344 The average and standard deviation of SWE field data and local scale EA outputs at the vegetative land cover types  
345 for all instances can be seen in Table 4. There were particularly notable SWE disparities at the end of April between peatbog  
346 and forest communities. As with snow depth, the average field and local scale SWE were lowest in December (34 and 35 mm),  
347 while they were highest in early April (177 and 187 mm), post-peak snow depth. Standard deviation increased over the period  
348 at both the field and local scale from  $\pm 6$  and  $\pm 5$  mm in December to  $\pm 46$  and  $\pm 33$  mm at the end of April. Across all instances  
349 the field SWE for coniferous forest (mineral soil), open area, and peatbog (wet) ranged from 30 to 173 mm, 34 to 176 mm,  
350 and 37 to 180 mm, respectively. Field SWE was repeatedly higher in transitional woodland/shrub (peat soil) ranging from 38  
351 to 192 mm. The exception was at the end of April when the inverse occurred, and it recorded the lowest SWE (119 mm)  
352 alongside the highest standard deviation of  $\pm 80$  mm that was influenced by extreme SWE field data variation. At the local  
353 scale, SWE continually ranged higher at coniferous forest (peat soil) from 36 to 191 mm than at coniferous forest (mineral  
354 soil) from 29 to 185 mm, despite the lack of on-the-ground data for the former. At the end of April, the difference increased  
355 to 19 mm. For both broad-leaved forest and transitional woodland/shrub, the opposite was found with SWE values tending to  
356 be higher in mineral soil than in peat soil from January to the end of April. For broad-leaved forest the difference peaked at 6  
357 mm at the end of April, while for transitional woodland/shrub it was up to 18 mm in both March and the end of April. Local  
358 scale peatbog (dry) had higher or equal to average SWE than peatbog (wet) from January to end of April, ranging from 111 –  
359 181 mm, compared to 108 – 178 mm. In late April the difference widened to 20 mm. Local scale arable and open area contained  
360 continually higher SWE values than dry and wet peatbogs between January and late April. A distribution of SWE over the 10  
361 km<sup>2</sup> site for each instance from December 2022 – April 2023 can be seen in Fig 7, which illustrates where and how much SWE  
362 varied over time for the field data and EA-based local scale outputs.



363  
364

**Table 4: Mean and standard deviation (in parentheses) for SWE (mm) estimates per LULC with field data and at the local scale with EA. Blank values indicate no field data.**

	SWE field data						SWE estimates with EA					
	14-Dec-22	17-Jan-23	15-Feb-23	17-Mar-23	17-Apr-23	28-Apr-23	14-Dec-22	17-Jan-23	15-Feb-23	17-Mar-23	17-Apr-23	28-Apr-23
Arable							35 (7)	123 (15)	142 (8)	183 (14)	194 (11)	149 (35)
Broad-leaved forest (mineral soil)							35 (5)	123 (7)	139 (6)	194 (11)	193 (11)	167 (22)
Broad-leaved forest (peat soil)							36 (4)	120 (8)	140 (7)	190 (11)	191 (12)	161 (24)
Coniferous forest (mineral soil)	30 (7)	105 (9)	132 (17)	159 (11)	173 (19)	140 (34)	29 (6)	120 (10)	134 (7)	180 (14)	185 (14)	150 (24)
Coniferous forest (peat soil)							37 (3)	123 (5)	143 (4)	192 (8)	198 (8)	169 (17)
Open area	34 (9)	115 (12)	136 (22)	164 (26)	176 (44)	142 (55)	37 (5)	128 (11)	140 (6)	193 (19)	194 (14)	164 (24)
Peatbog (dry)							36 (2)	111 (8)	133 (6)	169 (12)	181 (12)	133 (25)
Peatbog (wet)	37 (3)	107 (13)	131 (14)	162 (21)	180 (17)	121 (45)	37 (2)	108 (10)	133 (8)	165 (17)	178 (15)	113 (29)
Transitional woodland /shrub (mineral soil)							36 (6)	130 (9)	142 (6)	201 (12)	198 (12)	172 (22)
Transitional woodland /shrub (peat soil)	38 (5)	120 (11)	137 (14)	183 (21)	182 (35)	119 (80)	38 (2)	117 (9)	141 (7)	183 (14)	194 (11)	154 (27)
All LULC	34 (6)	110 (11)	133 (15)	166 (18)	177 (23)	131 (46)	35 (5)	117 (11)	137 (8)	180 (18)	187 (15)	144 (33)

365

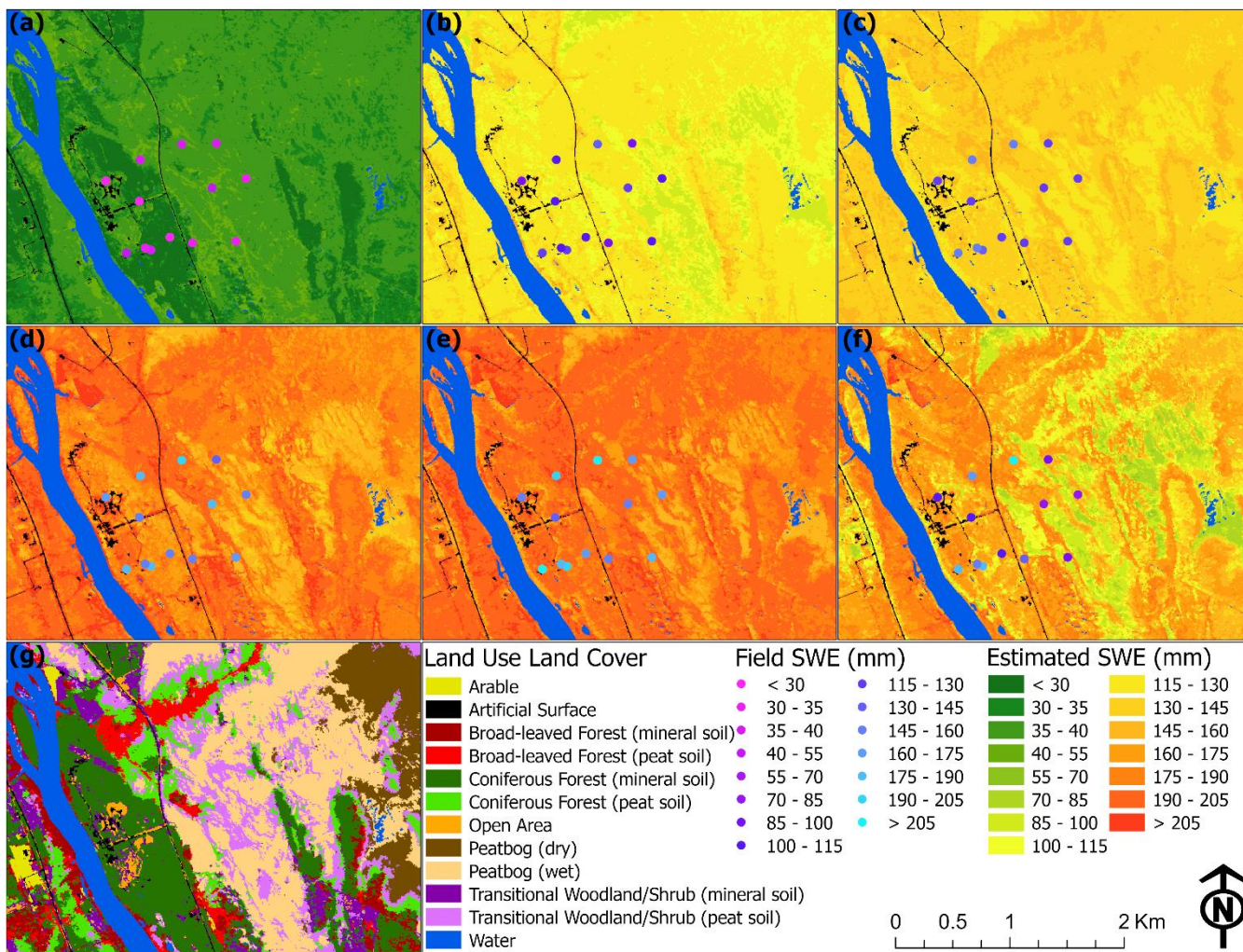


Figure 7: Field and estimated SWE (mm) in a) 14-December-22, b) 17-January-23, c) 15-February-23, d) 17-March-23, e) 17-April-23, and f) 28-April-23 alongside g) a LULC map based on data from CLC.

### 4.3 Snow density

Snow density is the ratio between the volume of water produced by melting a given volume of snow and the original volume of snow itself. This percentage refers to the water content within a given volume of snow. In general, fresh snowfall has low density while older, compacted, or wind-affected snow will have a higher density. Table 5 contains the mean and standard deviation of the snow density percentage for each vegetative landcover type from December to the end of April. The average snow density percentage for field and local scale data was lowest in December with 12% for both, while the highest was at the end of April at 36% and 39%, respectively. Standard deviation for the combined averages were generally low, with



377 a maximum of  $\pm 4\%$  and  $\pm 5\%$  in late April for field and local scale EA estimates. For the first five instances, snow density  
 378 percentages were slightly higher with the canopy-free open area and peatbog (wet), which ranged from 14 – 31% and 13 –  
 379 29%. In contrast, the more tree-covered coniferous forest (mineral soil) and transitional woodland/shrub (peat soil) routinely  
 380 experienced lower percentages ranging from 11 – 27% and 13 – 27%. In the final instance, field transitional woodland/shrub  
 381 (peat soil) and peatbog (wet) had the highest snow density percentages at 42% and 39%, while open area and coniferous forest  
 382 (mineral soil) were markedly lower at 33% and 32%.

383

384 **Table 5: Mean and standard deviation (in parentheses) for snow-to-water-percentage estimates per LULC with field data and EA.**  
 385 **Blank values indicate no field data.**

	Snow-water-percentage field data						Snow-water-percentage estimates with EA					
	14-Dec-22	17-Jan-23	15-Feb-23	17-Mar-23	17-Apr-23	28-Apr-23	14-Dec-22	17-Jan-23	15-Feb-23	17-Mar-23	17-Apr-23	28-Apr-23
Arable							12	20	23	24	29	42
							(2)	(2)	(2)	(2)	(2)	(8)
Broad-leaved forest (mineral soil)							11	21	23	25	27	41
							(1)	(2)	(1)	(2)	(2)	(7)
Broad-leaved forest (peat soil)							11	20	23	24	27	41
							(1)	(2)	(1)	(2)	(1)	(5)
Coniferous forest (mineral soil)	11	20	23	22	27	32	10	21	23	24	28	38
	(3)	(1)	(3)	(1)	(1)	(1)	(2)	(2)	(1)	(3)	(2)	(5)
Coniferous forest (peat soil)							12	20	23	24	28	41
							(1)	(1)	(1)	(1)	(1)	(3)
Open area	14	21	24	22	31	33	13	21	23	25	29	42.5
	(1)	(1)	(1)	(1)	(5)	(1)	(2)	(2)	(2)	(2)	(2)	(5)
Peatbog (dry)							12	19	23	23	29	37
							(1)	(1)	(1)	(1)	(1)	(4)
Peatbog (wet)	13	21	23	22	29	39	14	19	24	23	30	38
	(1)	(2)	(1)	(1)	(2)	(1)	(1)	(1)	(1)	(1)	(1)	(5)
Transitional woodland /shrub (mineral soil)							12	21	23	26	28	43
							(2)	(2)	(1)	(2)	(2)	(6)
Transitional woodland /shrub (peat soil)	13	20	23	23	27	42	13	19	23	23	28	40
	(2)	(1)	(1)	(1)	(1)	(1)	(1)	(1)	(1)	(1)	(1)	(4)



All LULC	12 (2)	20 (1)	23 (2)	22 (1)	28 (3)	36 (4)	12 (2)	20 (2)	23 (1)	24 (2)	28 (2)	39 (5)
----------	-----------	-----------	-----------	-----------	-----------	-----------	-----------	-----------	-----------	-----------	-----------	-----------

386

387

388

389

390

391

392

393

394

395

396

397

398

399

As with the field averages, for the local scale averages from December to early April there were generally minimal differences in snow density between different land cover types while experiencing greater fluctuations at the end of April with a maximum difference of 6%. Local scale arable and open area contained the same averages in three instances with open area also having a 1% higher increase in snow density in three instances. Peatbog (wet) contained percentages equal or up to 2% higher than peatbog (dry) in all instances. Average snow density percentage on transitional woodland/shrub (mineral soil) was equal to or up to 3% higher than for peat soil from January to the end of April, with broad-leaved forest (mineral soil) being equal to the broad-leaved forest (peat soil) in four instances and up to 1% higher in the remaining two. For coniferous forest it was relatively stable between the mineral and peat soils until the end of April when the average was 38% for mineral soil and 41% for peat soil. At the end of April for the local scale, the lowest snow density averages were recorded for dry and wet peatbogs at 37% and 38%, alongside 38% for coniferous forest (mineral soil). In contrast, the highest average snow density percentages at the local scale were in transitional woodland/shrub (mineral soil) at 43%, along with both arable and open area at 42%. A spatial view of the gradual increase in the snow density percentage across the six instances with the rapid rise at the end of April can be seen in Fig 8.

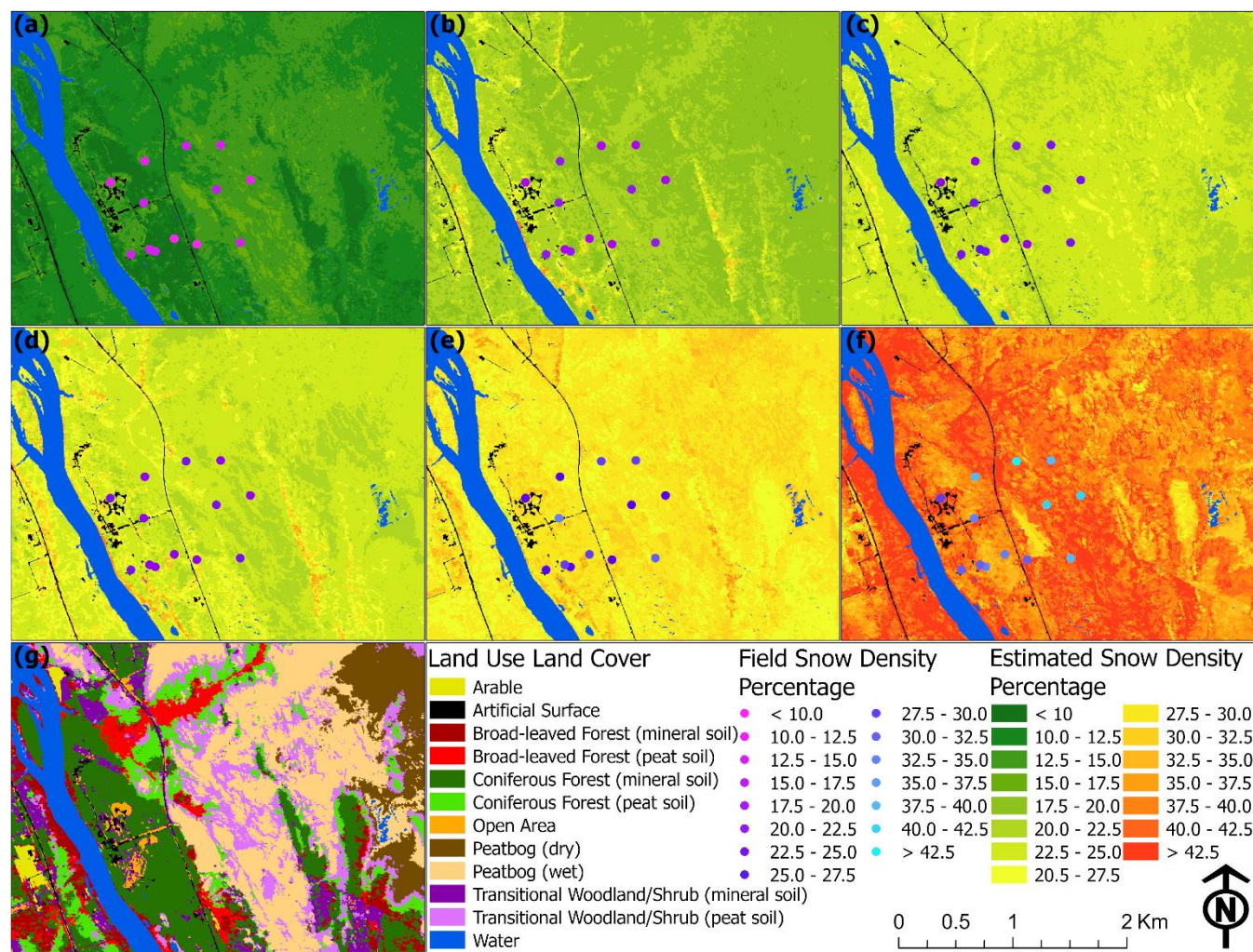


Figure 8: Field and estimated snow density percentage in a) 14-December-22, b) 17-January-23, c) 15-February-23, d) 17-March-23, e) 17-April-23, and f) 28-April-23 alongside g) a LULC map based on data from CLC.

## 5 Discussion

With snow depth estimation, all models performed well, with EA generating the best statistics. As is common for the study region the snow depth was lowest in December and highest in March before daily temperatures began exceeding 0 °C in April. There were consistent differences in snow depth between different vegetative communities. This was most apparent with higher snow depth being associated with broad-leaved forests, transitional woodland/shrubs, and particularly with coniferous forest (peat soil). Shallower snow depth was recorded at arable, coniferous forest (mineral soil), open areas, and both dry and wet peatbogs. With peatbogs, wet peat conducts heat better than dry peat resulting in heat flowing more effortlessly in wet peat layers in winter (Kujala et al., 2008), which may result in increased snowmelt and compaction.





411 Furthermore, mineral soil is more thermally conductive than peat soil (Atchley et al., 2016), which may promote snowmelt  
412 and compaction in similar vegetation communities containing mineral soil compared with peat soil where snowmelt and  
413 compaction would be reduced. Forests with drier mineral soils were generally more shielded from saturated soil found in  
414 peatbogs, while forests with peat soil were oftentimes adjacent to peatbogs. As the water table in many parts was at or near the  
415 surface, adjacent soils would contain greater soil saturation while the shielded mineral soils would in theory be more  
416 unsaturated. A notable exception is for approximately half of the broad-leaved forest (mineral soil) that is along the Kitinen  
417 River, which may have especially influenced snow depth, SWE, and snow density readings for that LULC. Given that saturated  
418 soil needs greater energy to heat than does unsaturated soil (Howe and Smith, 2021), saturated soil would require greater  
419 energy to warm in the spring and remain warmer in the winter than the unsaturated soil, which would have a resulting impact  
420 on snow cover. Post winter soil thaw varied with five FMI Campbell Scientific 109-L soil temperature sensors in the study  
421 area at 5 and 10 cm below the surface. For two sensors found in coniferous forest and one in an open area with mineral soil,  
422 the soil fully thawed out between 10 – 25 April, while for the two sensors in the peatland, the soil thawed out from 11 – 13  
423 May, which would have aided in accelerating overlaying snow cover melt for the former. It should be noted the impact that  
424 direct solar radiation may have on the energy balance of the snowpack and melt processes, along with wind impacted (open  
425 areas) versus wind protected (forest) vegetative communities. Lastly, snow interception and sublimation are major factors in  
426 forest communities, especially with conifers, which can lead to a notable diversity of snow accumulation on the forest floor  
427 (Helbig, 2020).

428 For the SWE estimations, model results were more mixed, but nonetheless promising. ANN, MLR, and EA were all  
429 able to produce encouraging metrics, while there was elevated variation with RF. EA consistently produced the best or second-  
430 best metrics, and generally produced the best metrics. MLR also performed well despite being the simplest form of machine  
431 learning in this study. In comparison to the snow depth there was a much smaller sample size which led to greater model  
432 uncertainty and disagreement. A greater number of SWE field samples would have provided enhanced findings; however,  
433 these field measurements can be time-consuming and expensive to collect across a large geographic region, with SWE  
434 measurements taking approximately 20 times as long to complete compared to snow depth measurements (Sturm et al., 2010).  
435 Nonetheless SWE was found to be lowest in December and highest in early April, which was post-peak snow depth. With the  
436 field data, it was found that SWE was higher in transitional woodland/shrub (peat soil) than with coniferous forest (mineral  
437 soil), which may be attributed to potentially more saturated peat soil allowing for greater water retention within the snow  
438 cover, while the unsaturated mineral soil drained slightly more liquid from the overlaying snow cover. Mineral soils across the  
439 study site are sand-rich and would be dry most of the time at the surface and likely never reach saturation, with any melted  
440 snow being drained in these soils. The one exception was with the end of April when there was a notable reversal, which may  
441 have been due to increased snow interception, snowmelt, sublimation, and windblown snow from branches in some vegetation  
442 types. A similar trend was observed at the local scale. Local scale coniferous forest (peat soil) continually contained higher  
443 average SWE than coniferous forest (mineral soil) which may be the result of the unsaturated mineral soil absorbing water  
444 from the overlaying snow while the saturated peat soil slowed the draining of water through the snowpack and into the soils.



445 Wet and dry peatbogs largely contained the lowest SWE measurements. These low open areas likely experienced enhanced  
446 wind activity that blew snow laterally away while also leading to greater sublimation. This would have led to greater snow  
447 particle cohesion and denser wind slab layer formation at the surface of the snowpack due to sintering after snow was mobilized  
448 in the wind (Mott et al., 2018).

449 Lastly, snow density was lowest in December and increased until the end of April when it was highest, which was  
450 during a period of rapid snowmelt. This was to be expected given that the beginning and middle winter typically contain larger  
451 quantities of fresh snowfall, while by the end of winter the snowpack would have compacted over time and become denser as  
452 the snowpack reaches an equilibrium temperature state of 0 °C (e.g., isothermal). As the snowpack develops, a larger snow  
453 grain size (depth hoar) results in a lower density in shallow snowpack. However, as the snowpack becomes isothermal, the  
454 depth hoar layer will metamorphose and become denser, especially near the ground (Gu et al., 2019). With the field data, a  
455 higher snow density percentage was observed at the end of April in peatbog (wet) and transitional woodland/shrub (peat soil)  
456 which contrasted with coniferous forest (mineral soil) and open area and may be attributed to soil saturation for those specific  
457 locations. At the end of April for the local scale the highest snow density percentages were found in vegetative communities  
458 that were more impacted by wind such as arable, open area, and transitional woodland/shrub (mineral soil) by a slight amount.  
459 In contrast, coniferous forest (mineral soil) along with wet and dry peatbogs contained the lowest percentages with landcover  
460 containing peat soil experiencing higher snow density percentages than with landcover containing mineral soil. Local scale  
461 wet peatbog was found to generally contain slightly higher amounts than dry peatbog. This may be attributed to dry peatbog  
462 being on average ~2.2 m higher in elevation than wet peatbog in our study area, which may have contributed to the movement  
463 of water over time to wet peatbogs at incrementally lower elevations.

464 Solar radiation increased throughout the timeframe and was not uniform over the study area, such as with thick forests  
465 sometimes obscuring adjacent canopy-free areas from solar radiation. As this would have impacted real-world snow estimates,  
466 we incorporated end of winter WV-2 imagery in the framework as it was able to aid in capturing such irregularities. A limited  
467 quantity and spatial extent of field measurements restricted further associations with vegetative communities, especially for  
468 SWE and, in turn, snow density. Had additional measurements been taken at communities missing field data, there would be  
469 a more comprehensive understanding of snow-landcover relationships. Additional datasets would have likely improved the  
470 model statistics and estimation of all three studied features. Soil moisture and air/subsurface temperature data were accessible  
471 in the study area yet were excluded, despite their strong association with snow depth and SWE (Contosta et al., 2016). This  
472 was due to a limited number of these measurements that corresponded to the six instances, with some containing gaps or  
473 missing data which would hinder spatial mapping and association with landcover types. Furthermore, very few of these  
474 measurements were located on or adjacent to the field snow depth and SWE measurements, which severely limited a proper  
475 linkage between the field data with soil moisture and temperature. Additional remote-sensing based data could have been  
476 utilized as an add-on to assist in mapping soil moisture and temperature for the study, alongside improving estimations for  
477 snow depth and SWE. However, due to the vegetative heterogeneity at the 10 km<sup>2</sup> site and clustering of the field data, medium  
478 and low-resolution imagery would have provided questionable benefit. High-resolution hyperspectral imagery and Synthetic



479 Aperture Radar (SAR) are particularly relevant, given the additional available spectral bands of the former and the proven  
480 application with snow depth and SWE detection in the latter (Patil et al., 2020), and would have likely benefited the findings.

## 481 **6 Conclusions**

482 We employed an object-based machine learning ensemble approach with time-series field snow depth and SWE data  
483 in northern Finland to first estimate snow depth at a local scale, before incorporating the snow depth outputs to estimate SWE  
484 at the same local scale alongside generating snow density estimations from six instances between December 2022 and April  
485 2023. Snow depth peaked in March, SWE peaked shortly after in early April, and snow density peaked with the final available  
486 data at the end of April. Multiple machine learning models, particularly with the ensemble approach, were shown to positively  
487 estimate key snowpack attributes over the period at the study site in Sodankylä. We established that there are direct spatial and  
488 temporal connections between three commonly studied snowpack elements with vegetation and soil types, with more research  
489 recommended to further characterize these associations. Although there is promise with intricate machine learning techniques,  
490 this study also highlights opportunities to assess where less complex methods may be employed for computational efficiency,  
491 especially when scaling up. While performed over a small portion of northern Finland, when matched with other field-based  
492 snowpack and remote sensing data across the region it would be possible to further upscale the studied snow-based estimates  
493 over a wider, regional-scale over various periods in time. This would also need to account for differing types of snowpack,  
494 terrain, and vegetative communities found throughout the pan-Arctic domain. As average temperatures around the Arctic are  
495 projected to increase with fewer days below freezing, more uncertain climactic conditions and precipitation events would  
496 affect the quantity, rate, and timing of snowfall, snow-on/snow-off, and snowmelt runoff in the region. Given that waterbodies  
497 such as lakes, ponds, and rivers in Finland and other high latitude areas are fed by the annual snowmelt, any changes to this  
498 natural process would meaningfully alter the hydrological makeup. The machine-learning based methodology applied in this  
499 effort can serve to benefit future snow-related analyses in high latitude regions, alongside other areas on Earth that regularly  
500 experience seasonal snow.

501 *Data availability.* Field snow depth and snow water equivalent data is maintained by the Finnish Meteorological Institute and  
502 is available at <https://litdb.fmi.fi/index.php>. Additional study data is available upon reasonable request.

503 *Author contributions.* DB, LVB, EJD, and TAD designed and initiated the study. RRB classified vegetation. EJD obtained  
504 LiDAR data. JL obtained field snow observations. DB, LVB, and EJD developed the methodology. DB wrote the initial draft  
505 and figures. All authors contributed to manuscript development and review.

506 *Competing interests.* The authors declare that they have no conflict of interest.

507 *Acknowledgements.* Staff at the Finnish Meteorological Institute are acknowledged for providing field measurements.



508 *Financial support.* This research was funded by the US Department of Defense - PE 0602144A Program Increase 'Defense  
509 Resiliency Platform Against Extreme Cold Weather'.

## 510 **References**

- 511 Anttila, K., Manninen, T., Karjalainen, T., Lahtinen, P., Riihelä, A., and Siljamo, N.: The temporal and spatial variability in  
512 submeter scale surface roughness of seasonal snow in Sodankylä Finnish Lapland in 2009–2010, *JGR Atmospheres*,  
513 119, 9236–9252, doi:10.1002/2014JD021597, 2014.
- 514 Arenson, L., Colgan, W., and Marshall, H. P.: Physical, thermal, and mechanical properties of snow, ice, and permafrost, in:  
515 *Snow and Ice-Related Hazards, Risks, and Disasters*, Elsevier, 35–71, doi:10.1016/B978-0-12-817129-5.00007-X,  
516 2021.
- 517 Atchley, A. L., Coon, E. T., Painter, S. L., Harp, D. R., and Wilson, C. J.: Influences and interactions of inundation, peat, and  
518 snow on active layer thickness, *Geophysical Research Letters*, 43, 5116–5123, doi:10.1002/2016GL068550, 2016.
- 519 Aune-Lundberg, L. and Strand, G.-H.: The content and accuracy of the CORINE Land Cover dataset for Norway, *International*  
520 *Journal of Applied Earth Observation and Geoinformation*, 96, 102266, doi:10.1016/j.jag.2020.102266, 2021.
- 521 Bai, J., Heikkilä, A., and Zong, X.: Long-Term Variations of Global Solar Radiation and Atmospheric Constituents at  
522 Sodankylä in the Arctic, *Atmosphere*, 12, 749, doi:10.3390/atmos12060749, 2021.
- 523 Barnett, T. P., Adam, J. C., and Lettenmaier, D. P.: Potential impacts of a warming climate on water availability in snow-  
524 dominated regions, *Nature*, 438, 303–309, doi:10.1038/nature04141, 2005.
- 525 Bartsch, A., Bergstedt, H., Pointner, G., Muri, X., Rautiainen, K., Leppänen, L., Joly, K., Sokolov, A., Orekhov, P., Ehrlich,  
526 D., and Soininen, E. M.: Towards long-term records of rain-on-snow events across the Arctic from satellite data, *The*  
527 *Cryosphere*, 17, 889–915, doi:10.5194/tc-17-889-2023, 2023.
- 528 Bössinger, T.: The Geophysical Observatory in Sodankylä, Finland – past and present, *Hist. Geo Space. Sci.*, 12, 115–130,  
529 doi:10.5194/hgss-12-115-2021, 2021.
- 530 Brodylo, D., Douglas, T. A., and Zhang, C.: Quantification of active layer depth at multiple scales in Interior Alaska  
531 permafrost, *Environ. Res. Lett.*, 19, 034013, doi:10.1088/1748-9326/ad264b, 2024.
- 532 Brown, R. D., Smith, C., Derksen, C., and Mudryk, L.: Canadian In Situ Snow Cover Trends for 1955–2017 Including an  
533 Assessment of the Impact of Automation, *Atmosphere-Ocean*, 59, 77–92, doi:10.1080/07055900.2021.1911781,  
534 2021.
- 535 Broxton, P. D., Van Leeuwen, W. J. D., and Biederman, J. A.: Improving Snow Water Equivalent Maps With Machine  
536 Learning of Snow Survey and Lidar Measurements, *Water Resources Research*, 55, 3739–3757,  
537 doi:10.1029/2018WR024146, 2019.
- 538 Cammalleri, C., Barbosa, P., and Vogt, J. V.: Testing remote sensing estimates of snow water equivalent in the framework of  
539 the European Drought Observatory, *J. Appl. Rem. Sens.*, 16, doi:10.1117/1.JRS.16.014509, 2022.



- 540 Cimoli, E., Marcer, M., Vandecrux, B., Bøggild, C. E., Williams, G., and Simonsen, S. B.: Application of Low-Cost UASs  
541 and Digital Photogrammetry for High-Resolution Snow Depth Mapping in the Arctic, *Remote Sensing*, 9, 1144,  
542 doi:10.3390/rs9111144, 2017.
- 543 Collados-Lara, A.-J., Pulido-Velazquez, D., Pardo-Igúzquiza, E., and Alonso-González, E.: Estimation of the spatiotemporal  
544 dynamic of snow water equivalent at mountain range scale under data scarcity, *Science of The Total Environment*,  
545 741, 140485, doi:10.1016/j.scitotenv.2020.140485, 2020.
- 546 Colliander, A., Mousavi, M., Kimball, J. S., Miller, J. Z., and Burgin, M.: Spatial and temporal differences in surface and  
547 subsurface meltwater distribution over Greenland ice sheet using multi-frequency passive microwave observations,  
548 *Remote Sensing of Environment*, 295, 113705, doi:10.1016/j.rse.2023.113705, 2023.
- 549 Contosta, A. R., Burakowski, E. A., Varner, R. K., and Frey, S. D.: Winter soil respiration in a humid temperate forest: The  
550 roles of moisture, temperature, and snowpack, *JGR Biogeosciences*, 121, 3072–3088, doi:10.1002/2016JG003450,  
551 2016.
- 552 Deems, J. S., Painter, T. H., and Finnegan, D. C.: Lidar measurement of snow depth: a review, *J. Glaciol.*, 59, 467–479,  
553 doi:10.3189/2013JoG12J154, 2013.
- 554 Douglas, T. A. and Zhang, C.: Machine learning analyses of remote sensing measurements establish strong relationships  
555 between vegetation and snow depth in the boreal forest of Interior Alaska, *Environ. Res. Lett.*, 16, 065014,  
556 doi:10.1088/1748-9326/ac04d8, 2021.
- 557 El Oufir, M. K., Chokmani, K., El Alem, A., Agili, H., and Bernier, M.: Seasonal Snowpack Classification Based on Physical  
558 Properties Using Near-Infrared Proximal Hyperspectral Data, *Sensors*, 21, 5259, doi:10.3390/s21165259, 2021.
- 559 Essery, R., Kontu, A., Lemmetyinen, J., Dumont, M., and Ménard, C. B.: A 7-year dataset for driving and evaluating snow  
560 models at an Arctic site (Sodankylä, Finland), *Geosci. Instrum. Method. Data Syst.*, 5, 219–227, doi:10.5194/gi-5-  
561 219-2016, 2016.
- 562 FMI (Finnish Meteorological Institute): Weather and sea database, available at: [https://en.ilmatieteenlaitos.fi/download-](https://en.ilmatieteenlaitos.fi/download-observations)  
563 [observations](https://en.ilmatieteenlaitos.fi/download-observations), last accessed 14 December, 2024.
- 564 Fontrodona-Bach, A., Schaefli, B., Woods, R., Teuling, A. J., and Larsen, J. R.: NH-SWE: Northern Hemisphere Snow Water  
565 Equivalent dataset based on in situ snow depth time series, *Earth Syst. Sci. Data*, 15, 2577–2599, doi:10.5194/essd-  
566 15-2577-2023, 2023.
- 567 Gaitán, J. J., Bran, D., Oliva, G., Ciari, G., Nakamatsu, V., Salomone, J., Ferrante, D., Buono, G., Massara, V., Humano, G.,  
568 Celdrán, D., Opazo, W., and Maestre, F. T.: Evaluating the performance of multiple remote sensing indices to predict  
569 the spatial variability of ecosystem structure and functioning in Patagonian steppes, *Ecological Indicators*, 34, 181–  
570 191, doi:10.1016/j.ecolind.2013.05.007, 2013.
- 571 Goel, A., Goel, A. K., and Kumar, A.: The role of artificial neural network and machine learning in utilizing spatial  
572 information, *Spat. Inf. Res.*, 31, 275–285, doi:10.1007/s41324-022-00494-x, 2023.



- 573 Goldberg, K., Herrmann, I., Hochberg, U., and Rozenstein, O.: Generating Up-to-Date Crop Maps Optimized for Sentinel-2  
574 Imagery in Israel, *Remote Sensing*, 13, 3488, doi:10.3390/rs13173488, 2021.
- 575 Green, J., Kongoli, C., Prakash, A., Sturm, M., Duguay, C., and Li, S.: Quantifying the relationships between lake fraction,  
576 snow water equivalent and snow depth, and microwave brightness temperatures in an arctic tundra landscape, *Remote*  
577 *Sensing of Environment*, 127, 329–340, doi:10.1016/j.rse.2012.09.008, 2012.
- 578 Gu, L., Fan, X., Li, X., and Wei, Y.: Snow Depth Retrieval in Farmland Based on a Statistical Lookup Table from Passive  
579 Microwave Data in Northeast China, *Remote Sensing*, 11, 3037, doi:10.3390/rs11243037, 2019.
- 580 Helbig, N., Moeser, D., Teich, M., Vincent, L., Lejeune, Y., Sicart, J.-E., and Monnet, J.-M.: Snow processes in mountain  
581 forests: interception modeling for coarse-scale applications, *Hydrol. Earth Syst. Sci.*, 24, 2545–2560,  
582 doi:10.5194/hess-24-2545-2020, 2020.
- 583 Henkel, P., Koch, F., Appel, F., Bach, H., Prashch, M., Schmid, L., Schweizer, J., and Mauser, W.: Snow Water Equivalent of  
584 Dry Snow Derived From GNSS Carrier Phases, *IEEE Trans. Geosci. Remote Sensing*, 56, 3561–3572,  
585 doi:10.1109/TGRS.2018.2802494, 2018.
- 586 Hoopes, C. A., Castro, C. L., Behrangi, A., Ehsani, M. R., and Broxton, P.: Improving prediction of mountain snowfall in the  
587 southwestern United States using machine learning methods, *Meteorological Applications*, 30, e2153,  
588 doi:10.1002/met.2153, 2023.
- 589 Howe, J. A. and Smith, A. P.: The soil habitat, in: *Principles and Applications of Soil Microbiology*, Elsevier, 23–55,  
590 doi:10.1016/B978-0-12-820202-9.00002-2, 2021.
- 591 Hu, Y., Che, T., Dai, L., Zhu, Y., Xiao, L., Deng, J., and Li, X.: A long-term daily gridded snow depth dataset for the Northern  
592 Hemisphere from 1980 to 2019 based on machine learning, *Big Earth Data*, 1–28,  
593 doi:10.1080/20964471.2023.2177435, 2023.
- 594 Jacobs, J. M., Hunsaker, A. G., Sullivan, F. B., Palace, M., Burakowski, E. A., Herrick, C., and Cho, E.: Snow depth mapping  
595 with unpiloted aerial system lidar observations: a case study in Durham, New Hampshire, United States, *The*  
596 *Cryosphere*, 15, 1485–1500, doi:10.5194/tc-15-1485-2021, 2021.
- 597 Jonas, T., Marty, C., and Magnusson, J.: Estimating the snow water equivalent from snow depth measurements in the Swiss  
598 Alps, *Journal of Hydrology*, 378, 161–167, doi:10.1016/j.jhydrol.2009.09.021, 2009.
- 599 Kelly, R. E., Chang, A. T., Tsang, L., and Foster, J. L.: A prototype AMSR-E global snow area and snow depth algorithm,  
600 *IEEE Trans. Geosci. Remote Sensing*, 41, 230–242, doi:10.1109/TGRS.2003.809118, 2003.
- 601 King, F., Kelly, R., and Fletcher, C. G.: New opportunities for low-cost LiDAR-derived snow depth estimates from a consumer  
602 drone-mounted smartphone, *Cold Regions Science and Technology*, 207, 103757,  
603 doi:10.1016/j.coldregions.2022.103757, 2023.
- 604 Kongoli, C., Key, J., and Smith, T.: Mapping of Snow Depth by Blending Satellite and In-Situ Data Using Two-Dimensional  
605 Optimal Interpolation—Application to AMSR2, *Remote Sensing*, 11, 3049, doi:10.3390/rs11243049, 2019.



- 606 Kujala, K., Seppälä, M., and Holappa, T.: Physical properties of peat and palsa formation, *Cold Regions Science and*  
607 *Technology*, 52, 408–414, doi:10.1016/j.coldregions.2007.08.002, 2008.
- 608 Leppänen, L., Kontu, A., Hannula, H.-R., Sjöblom, H., and Pulliainen, J.: Sodankylä manual snow survey program, *Geosci.*  
609 *Instrum. Method. Data Syst.*, 5, 163–179, doi:10.5194/gi-5-163-2016, 2016.
- 610 Leppänen, L., Kontu, A., and Pulliainen, J.: Automated Measurements of Snow on the Ground in Sodankylä, *Geophysica*, 53,  
611 45–64, 2018.
- 612 Li, K., DeCost, B., Choudhary, K., Greenwood, M., and Hattrick-Simpers, J.: A critical examination of robustness and  
613 generalizability of machine learning prediction of materials properties, *npj Comput Mater*, 9, 55, doi:10.1038/s41524-  
614 023-01012-9, 2023.
- 615 Lu, X., Hu, Y., Zeng, X., Stamnes, S. A., Neuman, T. A., Kurtz, N. T., Yang, Y., Zhai, P.-W., Gao, M., Sun, W., Xu, K., Liu,  
616 Z., Omar, A. H., Baize, R. R., Rogers, L. J., Mitchell, B. O., Stamnes, K., Huang, Y., Chen, N., Weimer, C., Lee, J.,  
617 and Fair, Z.: Deriving Snow Depth From ICESat-2 Lidar Multiple Scattering Measurements: Uncertainty Analyses,  
618 *Front. Remote Sens.*, 3, 891481, doi:10.3389/frsen.2022.891481, 2022.
- 619 Marti, R., Gascoin, S., Berthier, E., De Pinel, M., Houet, T., and Laffly, D.: Mapping snow depth in open alpine terrain from  
620 stereo satellite imagery, *The Cryosphere*, 10, 1361–1380, doi:10.5194/tc-10-1361-2016, 2016.
- 621 Meinander, O., Kontu, A., Kouznetsov, R., and Sofiev, M.: Snow Samples Combined With Long-Range Transport Modeling  
622 to Reveal the Origin and Temporal Variability of Black Carbon in Seasonal Snow in Sodankylä (67°N), *Front. Earth*  
623 *Sci.*, 8, 153, doi:10.3389/feart.2020.00153, 2020.
- 624 Mott, R., Vionnet, V., and Grünewald, T.: The Seasonal Snow Cover Dynamics: Review on Wind-Driven Coupling Processes,  
625 *Front. Earth Sci.*, 6, 197, doi:10.3389/feart.2018.00197, 2018.
- 626 Muskett, R. R.: Remote Sensing, Model-Derived and Ground Measurements of Snow Water Equivalent and Snow Density in  
627 Alaska, *IJG*, 03, 1127–1136, doi:10.4236/ijg.2012.35114, 2012.
- 628 Nagler, T. and Rott, H.: Retrieval of wet snow by means of multitemporal SAR data, *IEEE Trans. Geosci. Remote Sensing*,  
629 38, 754–765, doi:10.1109/36.842004, 2000.
- 630 Nadjla, B., Assia, S., and Ahmed, Z.: Contribution of spectral indices of chlorophyll (RECI and GCI) in the analysis of multi-  
631 temporal mutations of cultivated land in the Mostaganem plateau, in: 2022 7th International Conference on Image  
632 and Signal Processing and their Applications (ISPA), 2022 7th International Conference on Image and Signal  
633 Processing and their Applications (ISPA), Mostaganem, Algeria, 1–6, doi:10.1109/ISPA54004.2022.9786326, 2022.
- 634 Nienow, P. W. and Campbell, F.: Stratigraphy of Snowpacks, in: *Encyclopedia of Snow, Ice and Glaciers*, edited by: Singh,  
635 V. P., Singh, P., and Haritashya, U. K., Springer Netherlands, Dordrecht, 1081–1084, doi:10.1007/978-90-481-2642-  
636 2\_541, 2011.
- 637 Nolin, A. W.: Recent advances in remote sensing of seasonal snow, *J. Glaciol.*, 56, 1141–1150,  
638 doi:10.3189/002214311796406077, 2010.



- 639 Ntokas, K. F. F., Odry, J., Boucher, M.-A., and Garnaud, C.: Investigating ANN architectures and training to estimate snow  
640 water equivalent from snow depth, *Hydrol. Earth Syst. Sci.*, 25, 3017–3040, doi:10.5194/hess-25-3017-2021, 2021.
- 641 Pan, J., Durand, M. T., Vander Jagt, B. J., and Liu, D.: Application of a Markov Chain Monte Carlo algorithm for snow water  
642 equivalent retrieval from passive microwave measurements, *Remote Sensing of Environment*, 192, 150–165,  
643 doi:10.1016/j.rse.2017.02.006, 2017.
- 644 Patil, A., Singh, G., and Rüdiger, C.: Retrieval of Snow Depth and Snow Water Equivalent Using Dual Polarization SAR Data,  
645 *Remote Sensing*, 12, 1183, doi:10.3390/rs12071183, 2020.
- 646 Pes, B.: Ensemble feature selection for high-dimensional data: a stability analysis across multiple domains, *Neural Comput &*  
647 *Applic*, 32, 5951–5973, doi:10.1007/s00521-019-04082-3, 2020.
- 648 Prowse, T. D. and Owens, I. F.: Characteristics of Snowfalls, Snow Metamorphism, and Snowpack Structure with Implications  
649 for Avalanching, Craigieburn Range, New Zealand, *Arctic and Alpine Research*, 16, 107, doi:10.2307/1551176, 1984.
- 650 Pulliainen, J., Luojus, K., Derksen, C., Mudryk, L., Lemmetyinen, J., Salminen, M., Ikonen, J., Takala, M., Cohen, J.,  
651 Smolander, T., and Norberg, J.: Patterns and trends of Northern Hemisphere snow mass from 1980 to 2018, *Nature*,  
652 581, 294–298, doi:10.1038/s41586-020-2258-0, 2020.
- 653 Raghubanshi, S., Agrawal, R., and Rathore, B. P.: Enhanced snow cover mapping using object-based classification and  
654 normalized difference snow index (NDSI), *Earth Sci Inform*, 16, 2813–2824, doi:10.1007/s12145-023-01077-6,  
655 2023.
- 656 Rautiainen, K., Lemmetyinen, J., Schwank, M., Kontu, A., Ménard, C. B., Mätzler, C., Drusch, M., Wiesmann, A., Ikonen, J.,  
657 and Pulliainen, J.: Detection of soil freezing from L-band passive microwave observations, *Remote Sensing of*  
658 *Environment*, 147, 206–218, doi:10.1016/j.rse.2014.03.007, 2014.
- 659 Rodell, M. and Houser, P. R.: Updating a Land Surface Model with MODIS-Derived Snow Cover, *Journal of*  
660 *Hydrometeorology*, 5, 1064–1075, doi:10.1175/JHM-395.1, 2004.
- 661 Salzmann, N., Huggel, C., Rohrer, M., and Stoffel, M.: Data and knowledge gaps in glacier, snow and related runoff research  
662 – A climate change adaptation perspective, *Journal of Hydrology*, 518, 225–234, doi:10.1016/j.jhydrol.2014.05.058,  
663 2014.
- 664 Santi, E., Brogioni, M., Leduc-Leballeur, M., Macelloni, G., Montomoli, F., Pampaloni, P., Lemmetyinen, J., Cohen, J., Rott,  
665 H., Nagler, T., Derksen, C., King, J., Rutter, N., Essery, R., Menard, C., Sandells, M., and Kern, M.: Exploiting the  
666 ANN Potential in Estimating Snow Depth and Snow Water Equivalent From the Airborne SnowSAR Data at X- and  
667 Ku-Bands, *IEEE Trans. Geosci. Remote Sensing*, 60, 1–16, doi:10.1109/TGRS.2021.3086893, 2022.
- 668 Seibert, J., Jenicek, M., Huss, M., and Ewen, T.: Snow and Ice in the Hydrosphere, in: *Snow and Ice-Related Hazards, Risks,*  
669 *and Disasters*, Elsevier, 99–137, doi:10.1016/B978-0-12-394849-6.00004-4, 2015.
- 670 Stillinger, T., Rittger, K., Raleigh, M. S., Michell, A., Davis, R. E., and Bair, E. H.: Landsat, MODIS, and VIIRS snow cover  
671 mapping algorithm performance as validated by airborne lidar datasets, *The Cryosphere*, 17, 567–590, doi:10.5194/tc-  
672 17-567-2023, 2023.





- 673 Sturm, M., Taras, B., Liston, G. E., Derksen, C., Jonas, T., and Lea, J.: Estimating Snow Water Equivalent Using Snow Depth  
674 Data and Climate Classes, *Journal of Hydrometeorology*, 11, 1380–1394, doi:10.1175/2010JHM1202.1, 2010.
- 675 Tanniru, S. and Ramsankaran, R.: Passive Microwave Remote Sensing of Snow Depth: Techniques, Challenges and Future  
676 Directions, *Remote Sensing*, 15, 1052, doi:10.3390/rs15041052, 2023.
- 677 Tsai, Y.-L. S., Dietz, A., Oppelt, N., and Kuenzer, C.: Remote Sensing of Snow Cover Using Spaceborne SAR: A Review,  
678 *Remote Sensing*, 11, 1456, <https://doi.org/10.3390/rs11121456>, 2019.
- 679 Tuttle, S. E. and Jacobs, J. M.: Enhanced Identification of Snow Melt and Refreeze Events From Passive Microwave Brightness  
680 Temperature Using Air Temperature, *Water Resources Research*, 55, 3248–3265, doi:10.1029/2018WR023995,  
681 2019.
- 682 Venäläinen, P., Luojus, K., Mortimer, C., Lemmetyinen, J., Pulliainen, J., Takala, M., Moisander, M., and Zschenderlein, L.:  
683 Implementing spatially and temporally varying snow densities into the GlobSnow snow water equivalent retrieval,  
684 *The Cryosphere*, 17, 719–736, doi:10.5194/tc-17-719-2023, 2023.
- 685 Xu, Y., Jones, A., and Rhoades, A.: A quantitative method to decompose SWE differences between regional climate models  
686 and reanalysis datasets, *Sci Rep*, 9, 16520, doi:10.1038/s41598-019-52880-5, 2019.
- 687 Xue, J. and Su, B.: Significant Remote Sensing Vegetation Indices: A Review of Developments and Applications, *Journal of*  
688 *Sensors*, 2017, 1–17, doi:10.1155/2017/1353691, 2017.
- 689 Yang, J., Jiang, L., Luojus, K., Pan, J., Lemmetyinen, J., Takala, M., and Wu, S.: Snow depth estimation and historical data  
690 reconstruction over China based on a random forest machine learning approach, *The Cryosphere*, 14, 1763–1778,  
691 doi:10.5194/tc-14-1763-2020, 2020.
- 692 Yu, M.-Y., Vasudevan, R., and Johnson-Roberson, M.: LiSnowNet: Real-time Snow Removal for LiDAR Point Cloud,  
693 doi:10.48550/ARXIV.2211.10023, 2022.
- 694 Zhang, J., Pohjola, V. A., Pettersson, R., Norell, B., Marchand, W.-D., Clemenzi, I., and Gustafsson, D.: Improving the  
695 snowpack monitoring in the mountainous areas of Sweden from space: a machine learning approach, *Environ. Res.*  
696 *Lett.*, 16, 084007, doi:10.1088/1748-9326/abfe8d, 2021.
- 697 Zhao, W., Mu, C., Han, L., Sun, W., Sun, Y., and Zhang, T.: Spatial and temporal variability in snow density across the  
698 Northern Hemisphere, *CATENA*, 232, 107445, doi:10.1016/j.catena.2023.107445, 2023.